Chapter 1

Photovoltaic Concentrators and Building Integrated Photovoltaics

1.1 Introduction

Photovoltaic cells convert solar radiation directly into electricity. During four decades of research, photovoltaic devices, developed originally for space applications, have gradually found numerous terrestrial uses. Present photovoltaic technology can be characterised as:

- technically well proven with an expected service time of at least 30 years (Sick and Erge, 1996)
- a modular technology that can be employed for dispersed milliwatt to megawatt power generation in contrast to large central power stations (Green, 2000)
- a viable and cost effective option in remote site applications where the cost of grid extension or maintenance of a conventional power supply system is prohibitive (Anderson, 1997)
- accepted widely in building integrated applications (Sick and Erge, 1996)
- of low environmental impact suitable for deployment in the urban environment generating electricity at the point of use
- producing power over a wide range of insolation conditions, including the overcast skies prevalent in the UK (Hill et al., 1992)
- a potential major clean energy source, but not yet economically competitive for bulk power generation.

A PV solar concentrator increases insolation intensity at the PV surface, reducing the area of photovoltaic material required per unit power output. A cost reduction can be achieved for the overall photovoltaic/concentrator system when the concentrator cost is lower than the displaced PV material cost. Optical concentrators can be either reflective, refractive or a combination of both. Examples of reflective configurations are shown in figure 1.1.1.

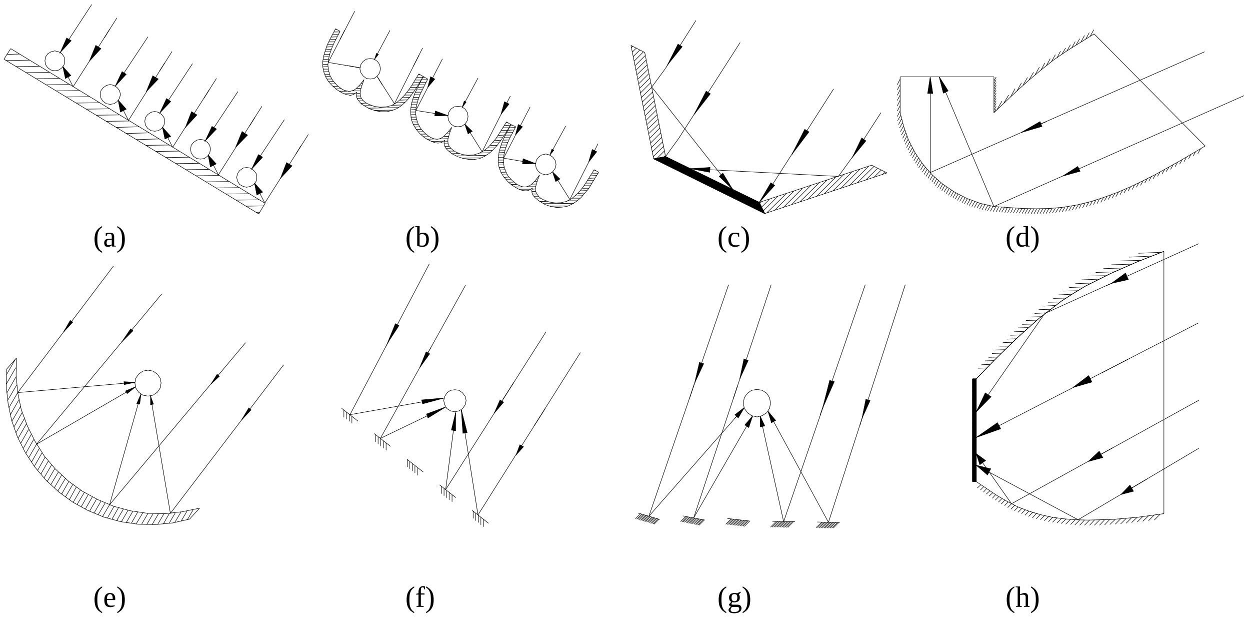

Figure 1.1.1 Possible concentrating reflector configurations: (a) tubular absorbers with diffuse back reflectors; (b) tubular absorbers with specular cusp reflectors; (c) plane receiver with plane reflectors; (d) plane receiver with inverted absorber CPC (e) parabolic concentrator; (f) Fresnel reflector; (g) array of heliostats with a central receiver (h) asymmetric compound parabolic concentrator.

This thesis presents a theoretical and experimental research investigation into the optics, heat transfer and overall system performance of an asymmetric compound parabolic photovoltaic concentrator (type h in figure 1.1.1) suitable for building integration in the UK climate.

1.2 Non-imaging Optics

Non-imaging optics provides effective and efficient collection, concentration, transport and distribution of energy in applications where image forming is unnecessary (Welford and Winston, 1979). In imaging optics an image is formed at the exit aperture or on a screen whereas for non-imaging optics no image of the object is formed (Winston, 1980). In an “ideal” non-imaging concentrator the first concentrator aperture is radiated uniformly from a Lambertian source. The absorber then receives a uniform flux (Leutz et al., 1999b). The Sun approximates to a Lambertian source, although its brightness is not uniform and its wavelength dependent brightness changes significantly across its disc. Practical non-imaging concentrators are designed with one or two pairs of acceptance half-angles, that accept light (for example, diffuse insolation) incident at angles other than the almost paraxial rays of the Sun. Concentrated solar fluxes are thus non uniform (Winston and Hinterberger, 1995) and flux densities at the absorber in a non-imaging solar concentrator are influenced by solar disk size and solar spectral irradiance (i.e. colour dispersion) (Leutz et al., 2000) and by the proportion of diffuse insolation particularly at low concentrations (Rabl, 1985).

For non-imaging optical systems the edge ray principle (Winston, 1974) applied to states that extreme rays entering a concentrating system through an entrance aperture must be extreme rays when leaving this system through another aperture (i.e. receiver or absorber) for maximal optical concentration.

Non-imaging systems can be made either by using a refracting lens or by using reflective mirrors (Boes and Luque, 1992). Fresnel lenses may offer flexibility in non-imaging optical design. For photovoltaics, uniformity of solar flux maintains electrical efficiencies by minimising electrical energy losses (Leutz et al., 1999b). Non-imaging Fresnel lenses allow uniformity of flux at the photovoltaic material to be achieved as manufacturing errors at the back and front faces of Fresnel lenses are partially self-correcting. In contrast an angular error in the plane of a mirror leads to twice this error in the reflected beam.

1.3 Compound Parabolic Concentrators

Developed originally for the detection of Cherenkov radiation in particle physics experiments (Hinterberger and Winston, 1966), a CPC for solar energy applications consists of two different parabolic reflectors that can reflect both direct and a fraction of the diffuse incident radiation at the entrance aperture onto the absorber in addition to the direct solar radiation absorbed directly by the absorber. The axis of the parabola makes an angle θ_a or $-\theta_a$ with the collector mid plane and its focus at P (or Q) as shown in figure 1.3.1 (Rabl, 1976a). The slope of the end point of the parabola is parallel to the collector mid plane. A CPC reflector shape can be designed in different ways according to the absorber shape. A basic form for a flat one-sided absorber is shown in figure 1.3.1.

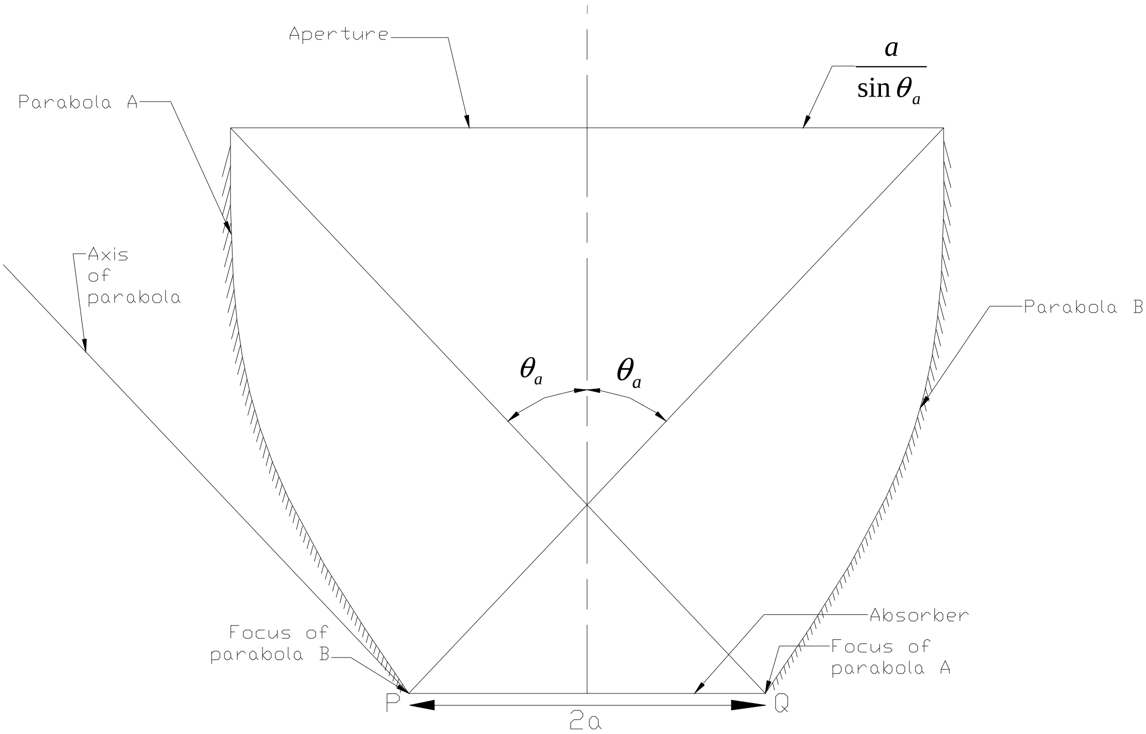

Figure 1.3.1 Schematic diagram of a Compound parabolic concentrator (Rabl, 1976a).

1.3.1 **The Equation of a CPC with a Flat Absorber**

For the co-ordinates in Figure 1.3.1.1, by rotation of the axis and translation of the origin, in terms of the diameter (2a) and the acceptance angle (θ_{max}), the equation for a meridian section CPC reflector is (Welford, 1978);

$$(r\cos\theta_{max} + y\sin\theta_{max})^2 + 2a(1+\sin\theta_{max})^2 r - 2a \cos\theta_{max}(2+\sin\theta_{max})z - a^2(1+\sin\theta_{max})(3+\sin\theta_{max}) = 0 \qquad (1.3.1.1)$$

In polar co-ordinates, the complete parametric equation becomes (Welford, 1978)

$$\left.\begin{array}{l} r = \dfrac{2f\sin(\theta-\theta_{max})}{1-\cos\theta} - a'; \quad z = \dfrac{2f\cos(\theta-\theta_{max})}{1-\cos\theta} \\ where \\ f = a'(1+\sin\theta_{max}) \end{array}\right\} \qquad (1.3.1.2)$$

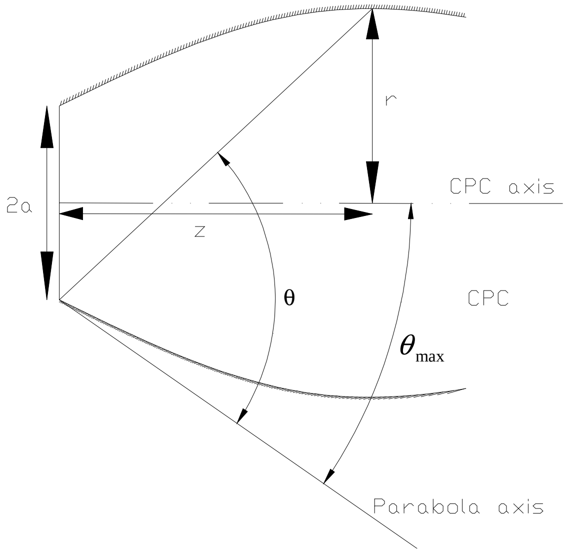

Figure 1.3.1.1 The angle θ used in the parametric equations of the CPC (Welford, 1978).

1.3.2 Limits to CPC Concentration

An attainable concentration limit follows from physical optics (Rabl, 1976a). The disk of the Sun subtends at the surface of the Earth an angle of $2\theta_s$ as shown in figure 1.3.2.1. Concentration is achieved by making a small image of the Sun with a given diameter optical device. Rays forming the smallest image make a cone with the largest semiangle φ. When the semi-angle of the image-forming cone is $\varphi=\pi/2$ the maximum theoretical limit for the concentration ratio is achieved (Winston and Welford, 1982) i.e. the area of the input aperture of the device divided by the area of the sun's image. In three dimensions the maximum concentration ratio is $C_{max} = \frac{1}{\sin^2 \theta_s}$, for a value of θ_s=0.27°, C_{max} is 45,031.

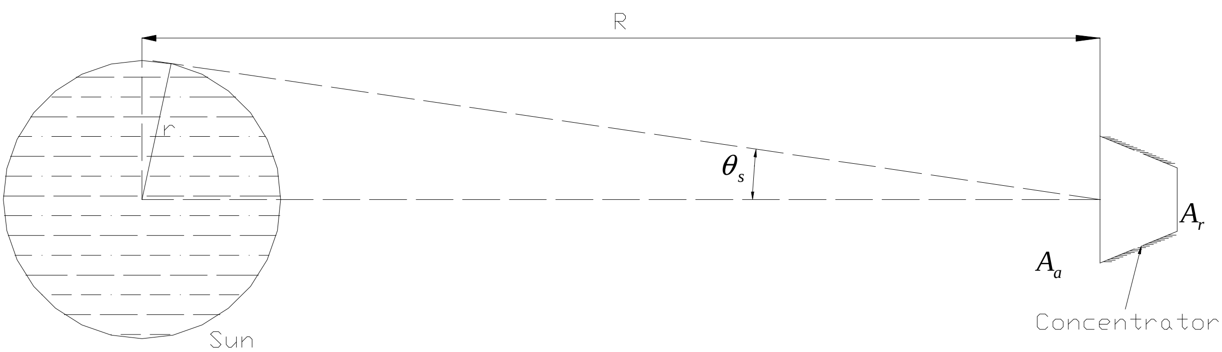

Figure 1.3.2.1 The half-angle subtended by the sun at a distance R from a concentrator with aperture area A_a and receiver area A_r (Rabl, 1985).

1.3.3 The Concentration Ratio of a CPC

The concentration ratio determines the increase in relative radiation at the surface of the exit aperture/absorber. The concentration ratio can be defined in several ways as described in section 1.3.3.1 to 1.3.3.3.

1.3.3.1 Area Concentration Ratio

The area concentration ratio is defined as the ratio of the area of aperture to the area of the receiver (Duffie and Beckmann, 1991) i.e. $C = \frac{A_a}{A_r}$. This ratio has an upper limit that depends on whether the concentrator is a three dimensional such as a paraboloid or a two dimensional such as compound parabolic concentrator. In terms of the half acceptance angle the concentration ratio is defined as (Rabl, 1976b)

$$\left.\begin{aligned} &C = \frac{1}{\sin\theta_S} && \text{for a two-dimensional system} \\ &C = \left(\frac{1}{\sin\theta_S}\right)^2 && \text{for a three-dimensional system} \end{aligned}\right\} \tag{1.3.3.1.1}$$

For reflective square pyramidal optical mixers, the concentration ratio becomes (O’Gallagher et al., 2002)

$$C = \left(\frac{A_a}{A_r}\right)^2 = \left(\frac{1}{\sin(\phi+\delta)}\right)^2 \tag{1.3.3.1.2}$$

1.3.3.2 Optical Concentration Ratio

The optical concentration ratio for an actual system is the proportion of incident rays within the collecting angle that emerge from the exit aperture. This yields an optical concentration ratio defined as (Winston, 1980)

$$C_{op} = \frac{G_{cs}}{G_{cns}} \tag{1.3.3.2.1}$$

1.3.4 Example of CPC Configurations for Selected Absorber Shapes

A CPC can be designed for different absorber shapes giving rise to a range of different reflector designs. The most common form of CPC is that based on a flat absorber with two parabolic reflectors either side. Four different CPC absorber shapes with their reflectors are shown in figure 1.3.4.1 (Rabl, 1976c). Figure 1.3.4.1(a) shows a CPC with a flat absorber for which solar energy incident within the acceptance half-angle is either incident directly at the flat absorber or reflected by the parabolic reflector and absorbed by the flat absorber. Figure 1.3.4.1(b) shows a CPC with a fin absorber which has a lower reflector area when compared to a CPC with a flat absorber. CPC’s can be formed with an “inverted-vee” shaped absorber as shown in figure 1.3.4.1(c), where both absorber planes are inclined along the acceptance-half angle's plane. This type of CPC also has a larger reflector surface area when compared to CPC's with a flat absorber. For the CPC with a tubular absorber shown in figure 1.3.4.1 (d), detailed parametric and experimental analysis of optics and heat transfer have been undertaken by Eames and Norton (1993a, 1993b, 1995).

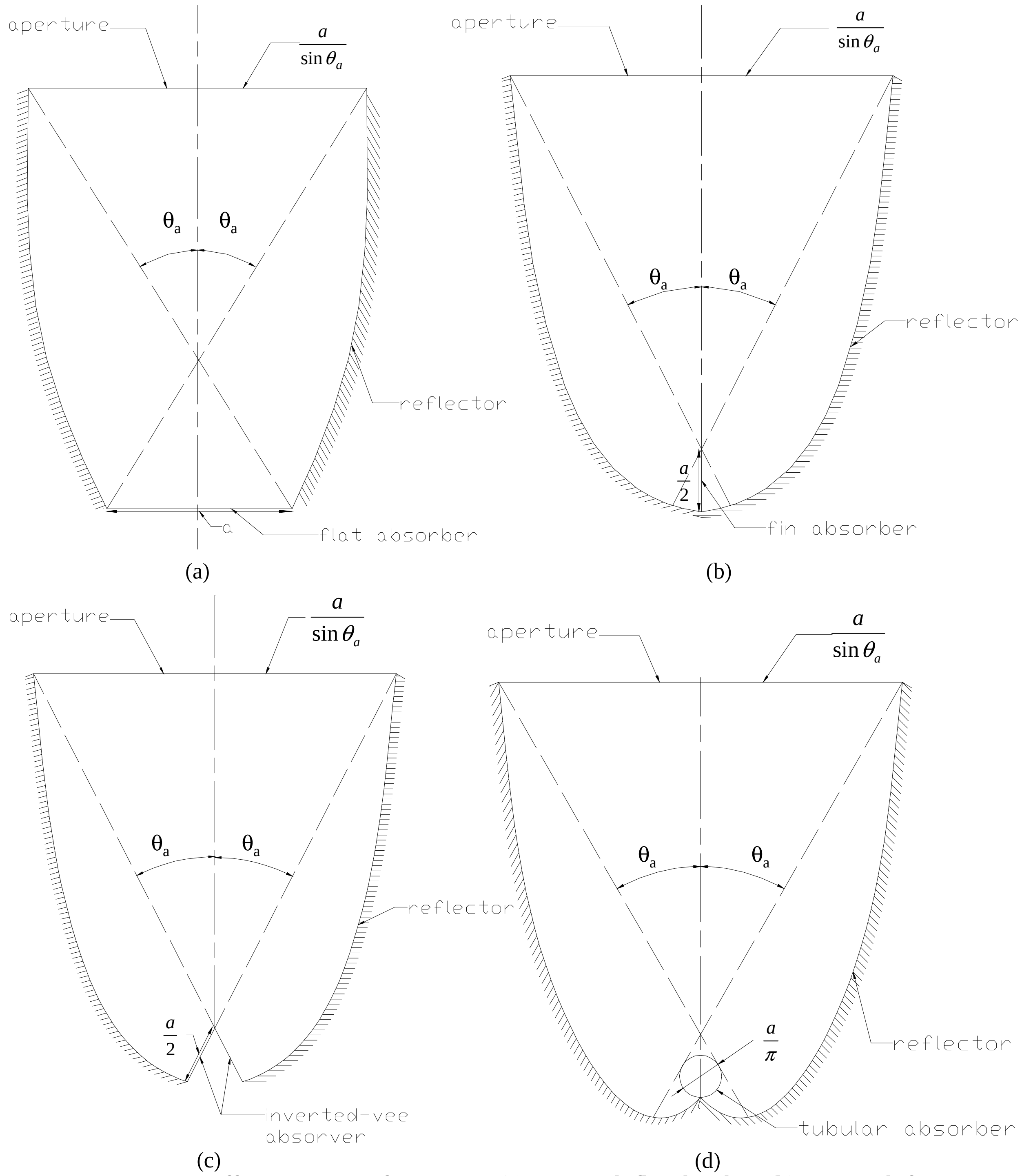

Figure 1.3.4.1 Different CPC configurations: (a) CPC with flat absorber, (b) CPC with fin, (c) CPC with "inverted vee" absorber, (d) CPC with tubular absorber (Gordon, 2001).

The thermal loss from the back of the absorber can be minimized by using a tubular absorber or a cusp reflector (O'Gallagher et al., 1980). An untruncated non-imaging cusp concentrator without a gap between the absorber and the collector cusp, with an acceptance angle $2\theta_a$ is shown in figure 1.3.4.2 and figure 1.3.4.3.

The distance I (θ) along the tangent from the receiver to the reflector can be calculated from

$$I(\theta) = r\theta \tag{1.3.4.1}$$

when $|\theta| \le \theta_a + \dfrac{\pi}{2}$.

for the involute sections of the curve and

$$I(\theta) = r\left(\frac{\theta + \theta_a + \dfrac{\pi}{2} - \cos(\theta - \theta_a)}{1 + \sin(\theta - \theta_a)}\right) \tag{1.3.4.2}$$

when $\theta_a + \pi/2 \le \theta \le \dfrac{3\pi}{2} - \theta_a$ for the reminder of the curve.

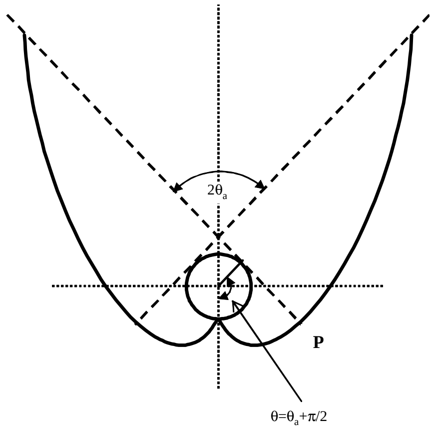

Figure 1.3.4.2 Non-imaging cusp concentrator with acceptance half angle θ_a (O'Gallagher et al., 1980).

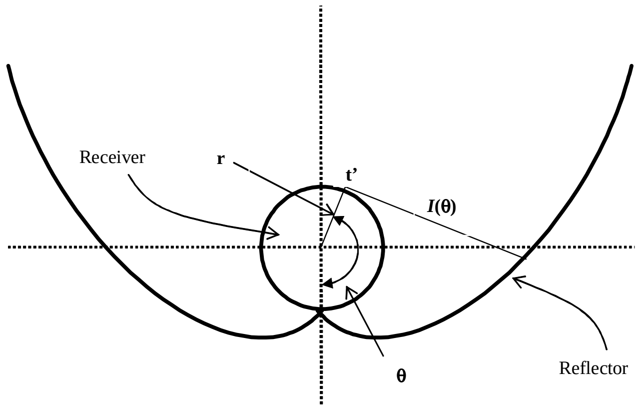

Figure 1.3.4.3 Elements used to generate mirror co-ordinates for ideal non-imaging cusp concentrator (O'Gallagher and Winston, 1983).

A gap as shown in figure 1.3.4.4 can be made between the receiver and the concentrator. For the configuration in figure 1.3.4.4 the tangent of length $I(\psi_0)$ from the cusp to the receiver made an angle at the centre of ψ_0 and in a similar manner the tangent of length $I(\psi)$ from the cusp to the receiver is subtending an angle of ψ at the receiver. Rearranging equations (1.3.4.1) and (1.3.4.2) gives

$$\mathrm{I}(\psi) = I(\psi_0) + r(\psi - \psi_0) \tag{1.3.4.3}$$

when $\psi_0 \le \psi \le \theta_a + \dfrac{\pi}{2}$ for the involute sections of the curve and

$$I(\psi) = \frac{2\left(I(\psi_0) - r\psi_0 + \left\{\dfrac{\pi}{2 + \theta_{subc}}\right\} r\right)}{1 + \sin(\psi - \theta_a)} \tag{1.3.4.4}$$

when $\theta_a + \pi/2 \le \psi \le \dfrac{3\pi}{2} - \theta_a$ for the remainder of the curve (O'Gallagher et al., 1980).

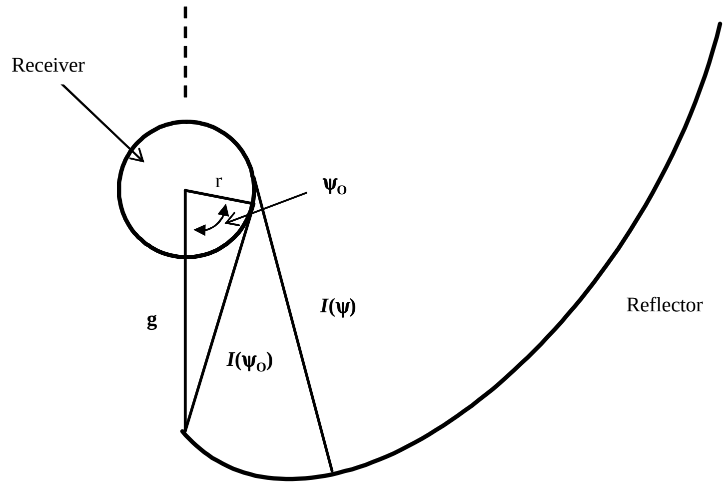

Figure 1.3.4.4 Schematic detail of non-imaging cusp concentrator geometry (O'Gallagher et al., 1980).

1.3.4.1 The Angular Acceptance of a CPC

The CPC has angular acceptance characteristics (Rabl, 1976a) such that all rays incident on the aperture within the acceptance angle, that is, with $\theta<\theta_a$ will reach the absorber, whereas all rays with $\theta>\theta_a$ will be travel back and fourth between the reflector sides to remerge eventually from the aperture. Figure 1.3.4.1.1 illustrates angular acceptance functions for a full and truncated CPC and a CPC with mirror error δ. The angular acceptance in figure 1.3.4.1.1 is the fraction of radiation incident on the aperture at angle θ that reaches the absorber for a CPC with acceptance half-angle θ_a and assumed reflectivity $\rho=1$. For an untruncated CPC the exit area a_{out} is given by $(1-\sin\theta)$. If the CPC is truncated, some rays outside the acceptance angle, i.e. having $\theta>\theta_a$, can reach the absorber (while, no rays with $\theta<\theta_a$ are rejected); this implies the inequality $a_{out}\leq(1-\sin\theta)$.

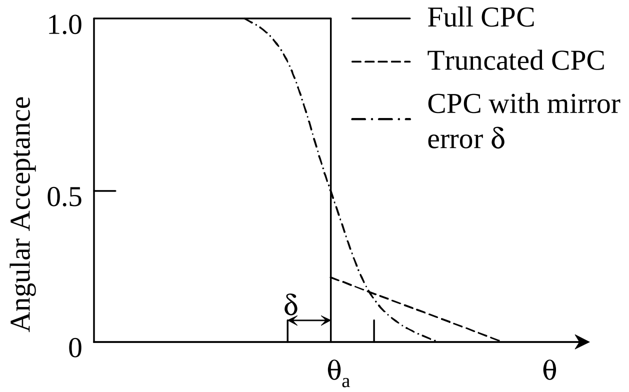

Figure 1.3.4.1.1 Angular acceptance function of untruncated CPC, truncated CPC and CPC with mirror error δ (Rabl, 1976a).

1.3.5 Asymmetric Compound Parabolic Concentrator (ACPC)

The foci and end points of the two parabolas of an ACPC make different angles with the absorber surface as shown in Figure 1.3.5.1. A is the aperture of the concentrator, R is the right parabola, L is the left parabola, F_R is the focus of R and F_L is focus of L. For the ACPC effective concentration ratio varies with the angle of incidence (Rabl, 1976a).

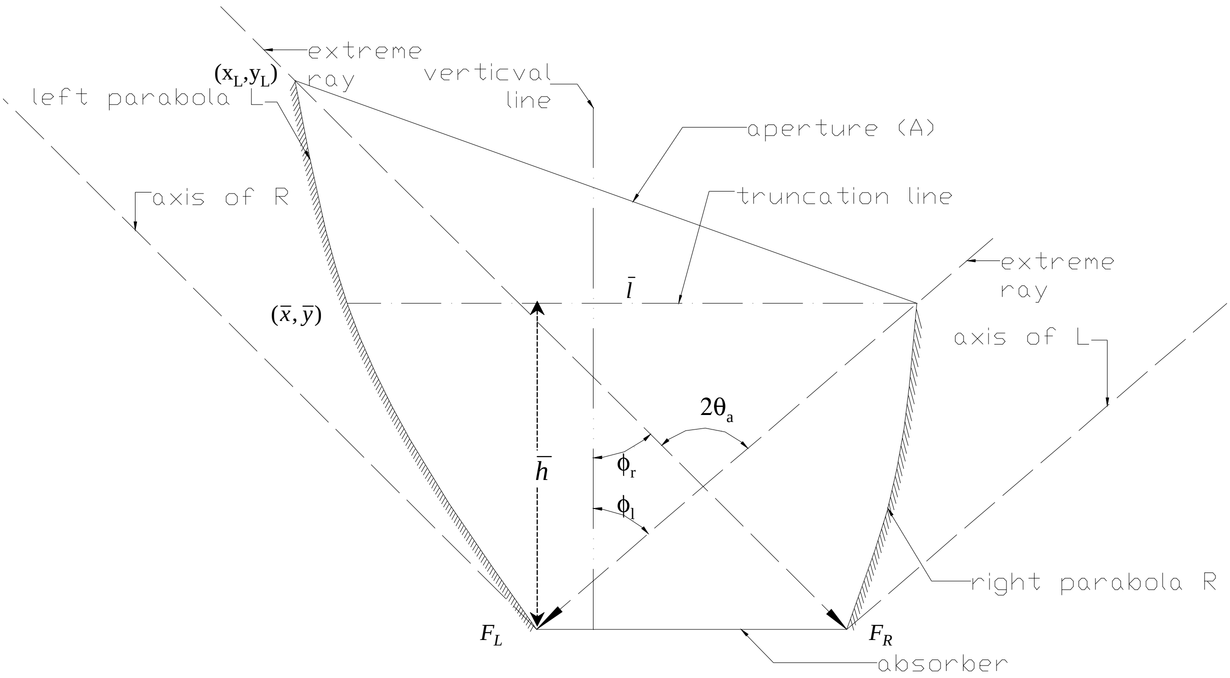

Figure 1.3.5.1 Asymmetric CPC with half acceptance angle $2\theta_a = \phi_l + \phi_r$ (Rabl, 1985).

Rabl (1976b) and Smith (1976) state that this type of concentrator has a maximum concentration ratio of $\left[Sin\left(\theta_{max}/2\right)\right]^{-1}$, where $\theta_{max}=\phi_l+\phi_r$. However Mills and Giutronich (1978) have shown that the maximum concentration ratio for a parabolic asymmetric concentrator is

$$C_{PA_{max}} = \left[\frac{1+Sin\phi_r}{\tan(\theta_{max}/2)} - \cos\phi_r\right]\left[\cos(\phi_r - \omega)^{-1}\right] \tag{1.3.5.1}$$

and the minimum concentration ratio is

$$C_{PA_{min}} = \left[\frac{1+\sin\phi_l}{\tan(\theta_{max}/2)} - \cos\phi_l\right] \tag{1.3.5.2}$$

where

$$\cos\omega = \frac{(\sin\theta_{max} - \cos\phi_r + \cos\phi_l)}{2\sqrt{(1-\cos\phi_l\cos\phi_r)}} \tag{1.3.5.3}$$

Truncation of the reflectors of an ACPC reduces the size and cost of a system but results in a loss of concentration. The degree of truncation for a given ACPC can be determined in terms of the co-ordinates of a full ACPC. As figure 1.3.5.1 illustrates, the left half of the ACPC is terminated at the point $(\bar{x}, \bar{y})$, instead of the end point (x_L, y_L) of the full ACPC. The right half of the ACPC, is of course, truncated in an analogous manner. Truncation does not change the absorber area. The width $(\bar{l})$, height $(\bar{h})$, and the position co-ordinates $(\bar{x})$ of the truncated ACPC are (Rabl 1976a)

$$\bar{l} = 2\bar{x}\cos\theta - \frac{\bar{x}^2}{s(1+\sin\theta)}\sin\theta + s\left(\sin\theta - \cos^2\theta\right) \tag{1.3.8.1}$$

$$\bar{h} = \bar{x}\sin\theta + \frac{\bar{x}^2\cos\theta}{2s(1+\sin\theta)} - \frac{s}{2}\cos\theta(1+\sin\theta) \tag{1.3.8.2}$$

and

$$\bar{x} = s\left[\frac{(1+\sin\theta)}{\cos\theta}\right]\left[-\sin\theta + \left(1+\frac{\bar{h}}{h}\cot^2\theta\right)^{\frac{1}{2}}\right] \tag{1.3.8.3}$$

1.3.5.1 **Different ACPC Configurations**

Asymmetric compound parabolic concentrator designs have been reported for different applications (Rabl 1976a, 1976b; Smith 1976; Mills and Giutronich 1978, 1979; Winston and Welford 1978; Blanco et al., 1986; Mullick et al., 1987; Kienzlen et al., 1988; Norton et al., 1991; Bezrukikh et at., 2003; Zacharopoulos et al., 2000; Adsten 2002 and Mallick et al., 2002a, 2002b). Asymmetrical compound parabolic reflectors have been designed to match annual needs and to accept a wide angular range of direct and diffuse solar radiation (Blanco et al., 1986; Mullick et al., 1987). A reverse flat-plate collector (RFPC) intended as a stationary asymmetric collector is shown in figures 1.3.5.1.1 and 1.3.5.1.2 (Kienzlen et al., 1988). An ideal extreme asymmetrical concentrator (EAC), shown in figure 1.3.5.1.3 (Smith, 1976), collects solar energy within the maximum acceptance half-angle at a fixed concentration. Asymmetrical concentrator geometry suggests that manufacturing costs could be high. The long second reflector leads to a large number of reflections being required for rays to reach the receiver, which implies higher optical losses and lower optical efficiency. In the subsequently developed EAC (Mills and Giutronich, 1979) based on the Winston-Hinterberger curve reflector shown in figure 1.3.5.1.4, the mirror is located relatively close to the receiver providing a larger acceptance angle for rays reflected from the mirror, reducing the number of reflections. This allows an increase in aperture area which compensates for losses due to rays passing through the gap between the receiver and mirror (Winston and Welford, 1978).

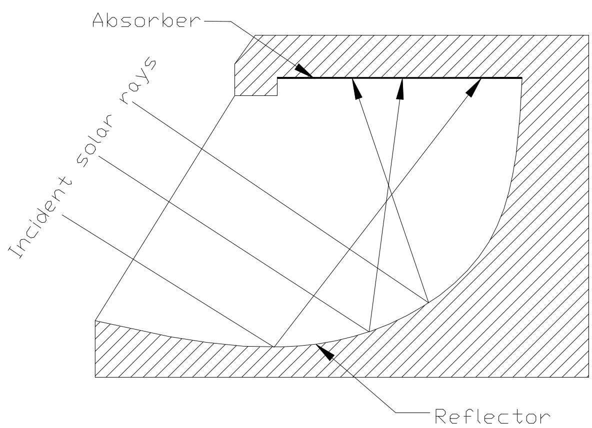

Figure 1.3.5.1.1 Schematic cross section of full version RFPC (Kienzlen et al., 1988).

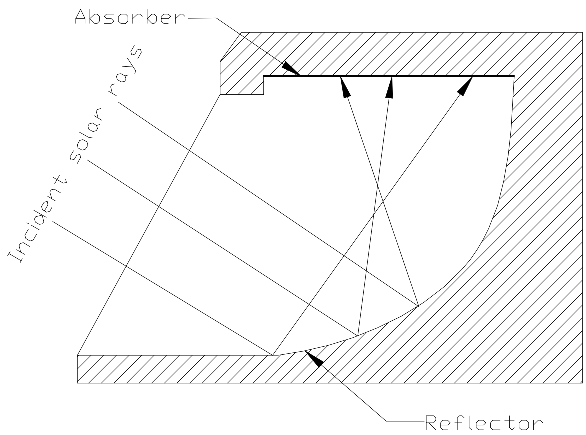

Figure 1.3.5.1.2 Schematic cross section of straightened version RFPC (Kienzlen et al., 1988).

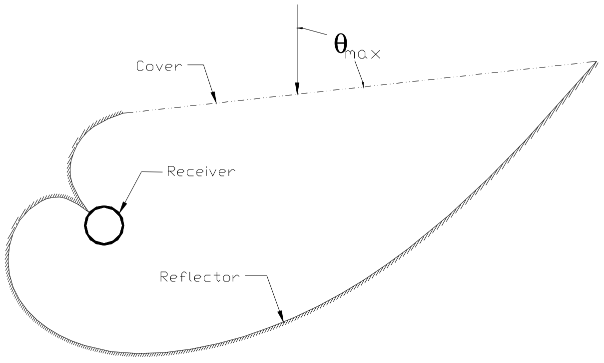

Figure 1.3.5.1.3 An ideal extreme asymmetrical concentrator (EAC) (Smith, 1976).

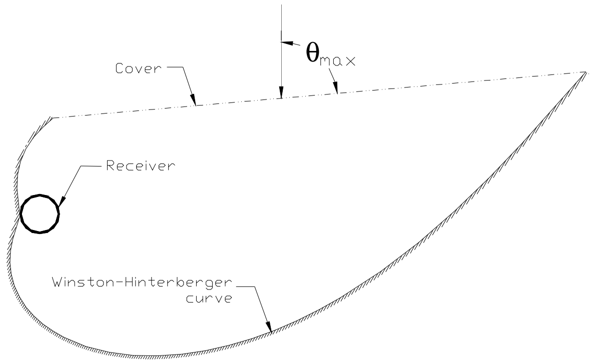

Figure 1.3.5.1.4 A nearly ideal EAC having the receiving tube well exposed to directions within the acceptance angle (Mills and Giutronich, 1979).

The ‘sea shell’ asymmetric concentrator with $2\theta_a=\phi_I$ and $\phi_r=0$ (Rabl, 1976b) is shown in figure 1.3.5.1.5 and figure 1.3.5.1.6. The system in figure 1.3.5.1.5 was designed for maximum output in summer and the system in figure 1.3.5.1.6 was designed to achieve maximum output in winter. The focus is at the edge of the absorber, a single parabola, CD, whose axis is parallel to one of the extreme rays, the parabola concentrates all radiation incident on the aperture with $|\theta|<\theta_a$ on the absorber. The ‘sea shell’ collector shown in figure 1.3.5.1.5 has an acceptance half-angle of 36° providing a collection time of seven hours.

The Maximum Reflector Collector (MaReCo) was characterised experimentally for high latitude solar thermal and bi-facial solar photovoltaics applications (Adsten, 2002). Different MaReCo configurations were made for stand-alone, roof integrated, east/west, spring/fall and wall integration. A cross section of a stand-alone MaReCo is shown in figure 1.3.5.1.7 (Adsten, 2002). Figure 1.3.5.1.8 illustrates that the cross section of roof integrated MaReCo designed for Stockholm conditions (Adsten, 2002). The highest optical efficiency reported was 56% for a bifacial based MaReCo. In contrast, the predicted optical efficiency of 81% was reported for dielectric filled PV covers (Zacharopoulos et al., 2000) and 85% for air filled asymmetric CPC PV system (Mallick et al., 2002a).

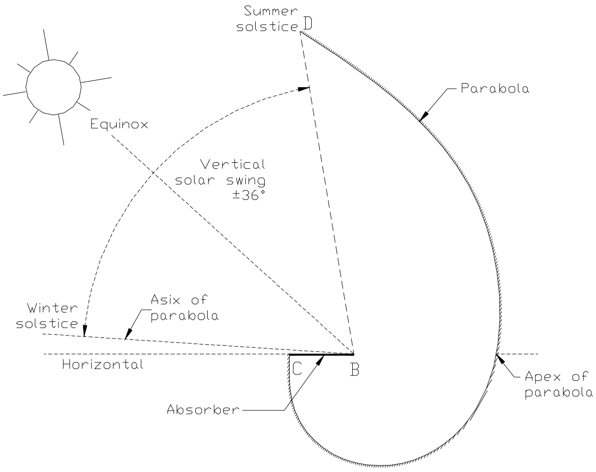

Figure 1.3.5.1.5 Stationary ‘Sea Shell’ collector with variable concentrations, with maximum output in the summer (Rabl, 1976b).

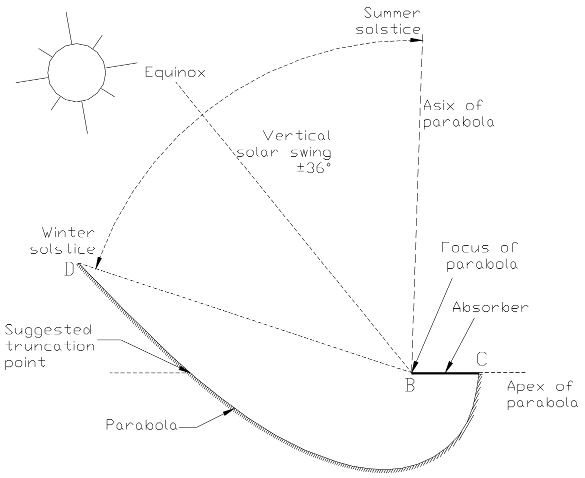

Figure 1.3.5.1.6 Stationary ‘Sea Shell’ collector with variable concentrations, with maximum output in the winter (Rabl, 1976b).

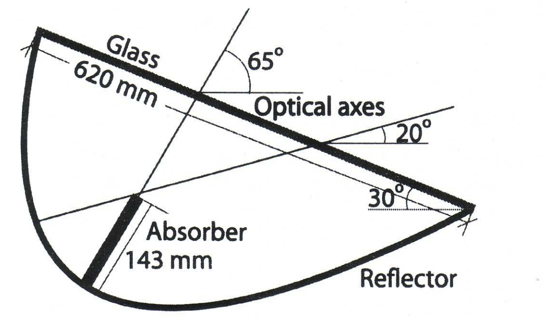

Figure 1.3.5.1.7 Section of the stand-alone MaReCo for Stockholm conditions. Aperture tilt 30°. Optical axes 20 and 65° defined from the horizon (Adsten, 2002).

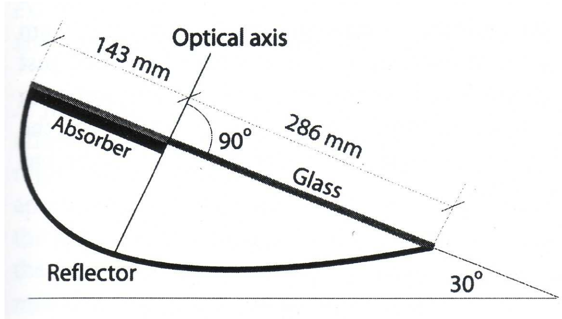

Figure 1.3.5.1.8 Section of a roof integrated MaReCo design for a roof angle of 30°. Optical axis perpendicular to the cover glass (Adsten, 2002).

1.3.6 **Photovoltaic Concentrators**

Solar cells are usually very expensive. An effective way of reducing the cost of photovoltaic systems is either by reducing solar cell manufacturing cost or illuminating solar cells with a higher light intensity than is available naturally. In the latter case solar cells convert the additional power incident without significant loss of efficiency. This can be done by either trapping light within screen-printed solar cells (Green, 1995) or using reflective/refractive devices to increase the luminous power flux on to the solar cell surface (Luque et al., 1995). A solar cell concentrator structure based on a $Ga_{0.83}In_{0.17}As$ bottom cell grown lattice mismatched on GaAs substrates with a highest efficiency of 31% at 300 suns and efficiencies greater then 29% at 1000 suns has been reported (Dimroth et al., 2000). Static parabolic trough concentrators for different receiver locations have been reported for photovoltaic applications (Kabakov and Levin, 1994). A one axis tracking parabolic trough mirror and a three dimensional second stage compound parabolic photovoltaic concentrator with a geometrical concentration ratio of 200 has achieved an electrical efficiency of 26% (Hein et al., 2003).

Non-imaging Fresnel lens concentrators for medium concentration photovoltaic applications have been designed, manufactured and a comparative cost analysis reported (Leutz et al., 1999a, 1999c). A truncated non-imaging Fresnel lens was analysed using a ray trace analysis (Welford, 1978) for minimal optical aberration. Fresnel lens photovoltaic concentrators have operated generally at comparatively high concentration ratios, with high solar cell temperatures and with a non-uniform flux distribution at the absorber. A theoretical and experimental analysis of hollow reflective pyramidal photovoltaic system reported that concentrator collection efficiencies of 100% can be achieved between 0º to 42.2º solar incidence angles (O'Gallagher et al., 2002). Variable acceptance half angle pairs have been designed for use with a non-imaging Fresnel lens for photovoltaic concentrator applications (Leutz et at., 2000). The optical concentration ratio undergoes a sharp decrease once the incidence angle exceeds the design acceptance half angle.

A non-imaging static concentrator lens was developed for the conditions in Sydney, Australia utilising refraction and total internal reflection to give a geometrical concentration ratio of 2.0 and a lens efficiency of 94% (Shaw and Wenham, 2000). The annual averaged optical concentration ratio was 1.88 for direct insolation within ±60º and ±25º in the East-West and North-South directions respectively.

A flat plate static concentrator (FPSC) with optical efficiencies of 87.6% and 85.6% was reported for mono-facial and bi-facial solar photovoltaic applications in Toyko, Japan (Uematsu et al., 2001a,). It was reported that 90% of the annual irradiation could be collected by the mono-facial system with a concentration ratio of 1.5 and the bifacial system with a concentration ratio of 2.0 (Uematsu et al., 2001b). Optical efficiencies of 94.4% (Uematsu et al., 2001c) based on a two-dimensional raytrace program were reported for the FPSC system with a prism array. The front and rear illumination efficiencies were reported to be 15% and 10.5% respectively (Uematsu et al., 2003). However Uematsu et al., (2001a, 2001b, 2001c) did not take into account the effect of increased temperatures on the photovoltaic solar cells.

Two linear dielectric non-imaging concentrating covers for PV integrated building façades were analysed using a three dimensional ray trace analysis (Zacharopoulos, 2001). Total internal reflection within the dielectric material provided optimal optical efficiency. A three dimensional optical analysis showed that the asymmetric concentrator design is more suitable for use in a building façade compared to a symmetric concentrator. Both concentrators had an optical efficiency of 81% for a wide range of solar incidence angles. The asymmetric concentrator maintained optical efficiencies of over 40% even for incidence angles outside its two-dimensional angular acceptance range. The symmetric and asymmetric dielectric covers were shown to collect 12000 $MJyear^{-1}m^{-2}$ and 10400 $MJyear^{-1}m^{-2}$ when located with a 70° inclination in Crete. The comparative energy collected by a symmetric dielectric concentrator and a flat plate cover are shown in figure 1.3.6.1 (Zacharopolous et al., 2000).

A prototype photovoltaic concentrator array called *Euclides* of 60.4 m^2 has been built using reflecting linear optics maintained in focus by horizontal single-axis tracking (Sala et al., 1996). The solar cells used in the prototype model were commercially available Saturn cells fabricated by BP Solar in Spain. The results from the *Ecluides* prototype showed a clear cost advantage with respect to flat modules. Efficiencies of 17% under 5× concentration have been achieved (Bruton et al., 2002).

Static concentrators offer a compromise between high concentration systems that require tracking and one-sun flat plate modules. A "slimline" design was reported to achieve a concentration ratio of four (Wenham et al., 1995). Thermal analysis indicated that performance loss through additional heating of the PV was more than offset by the gains achieved through concentration. The efficiency of the module was reported to be 15% greater than that of the flat plate module (Wenham et al., 1995). A high concentration parabolic dish for photovoltaic applications with a concentration of 1000 suns have been demonstrated as shown in figure 1.3.6.2 (Feuermann and Gordon, 2001).

Solar cells based on $Cu(In,Ga)Se_2$ with low concentration compound parabolic and plane reflectors for low concentration photovoltaic applications (Wennerberg et al., 2000; Brogren et al., 2003) gave a maximum electric power increase of 1.9 times and the fill factor decreased from 0.6 to 0.5 for systems without concentrator and with concentrator respectively (Brogren et al., 2003).

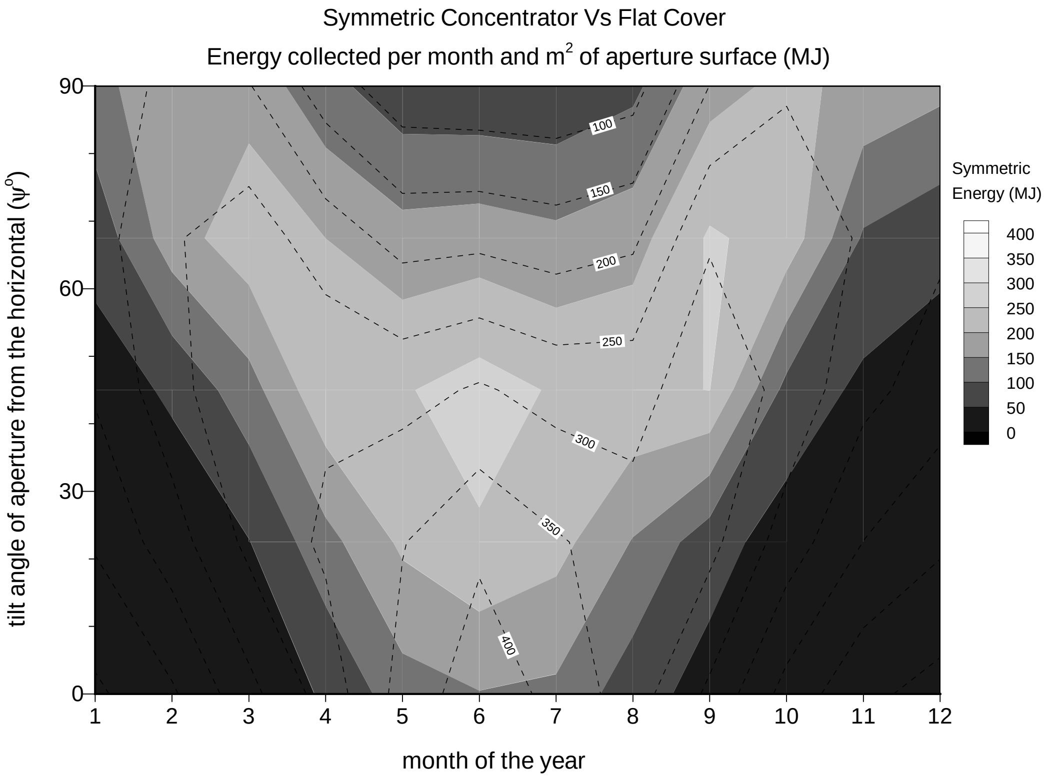

Figure 1.3.6.1 Energy collected per month and m^2 of the aperture surface for the symmetric concentrating (flood) and the flat (dashed line) covers against the tilt angle ψ from the horizontal. The covers are located in London, UK (52°N) and facing south (γ=0° and β=0°) (Zacharopoulos et al., 2000).

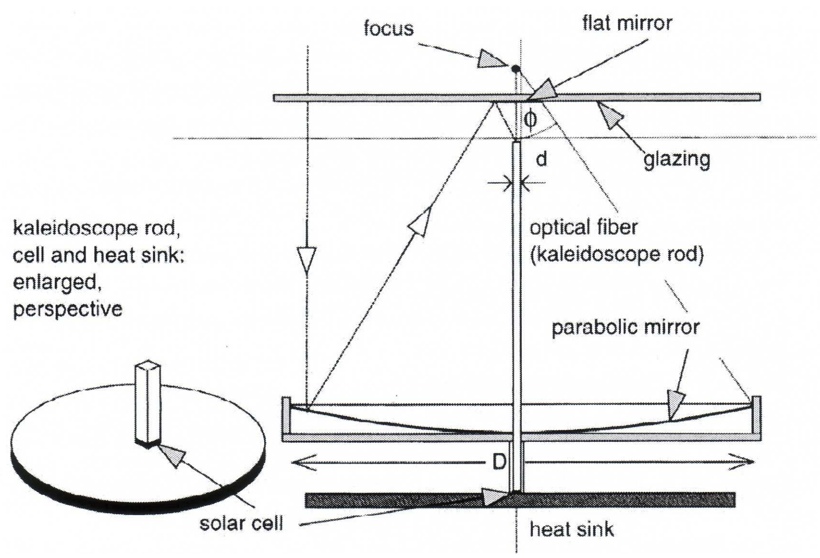

Figure 1.3.6.2 Schematic diagram of a solar mini-dish photovoltaic concentrator (Feuermann and Gordon, 2001).

1.3.6.1 **Luminescent and Quantum Dot Concentrators**

In the early 1970's fluorescent concentrators were first proposed (Andreev et al., 1997). In the fluorescent concentrator short wave solar radiation is absorbed by a dye, the dye then emits long-wave radiation isotropically, ideally with high quantum efficiency. This radiation is trapped within a sheet by internal reflection. The "trapped light" is converted at the edge of the sheet by a PV cell with band gap just below the luminescent energy (Taleb, 2002). Excess photon energy is dissipated by luminescent red shift rather than in the cell where the heat increase would reduce electrical efficiency. Such a non-optical solar concentrator can be made using quantum dots. Quantum dots are nanometre sized crystalline semiconductors as shown in figure 1.3.6.1.1. In the quantum dot concentrator, the luminescent dye is replaced by the quantum dots (Barnham et al., 2000). Quantum dots can be tuned to the absorption threshold by the choice of dot diameter.

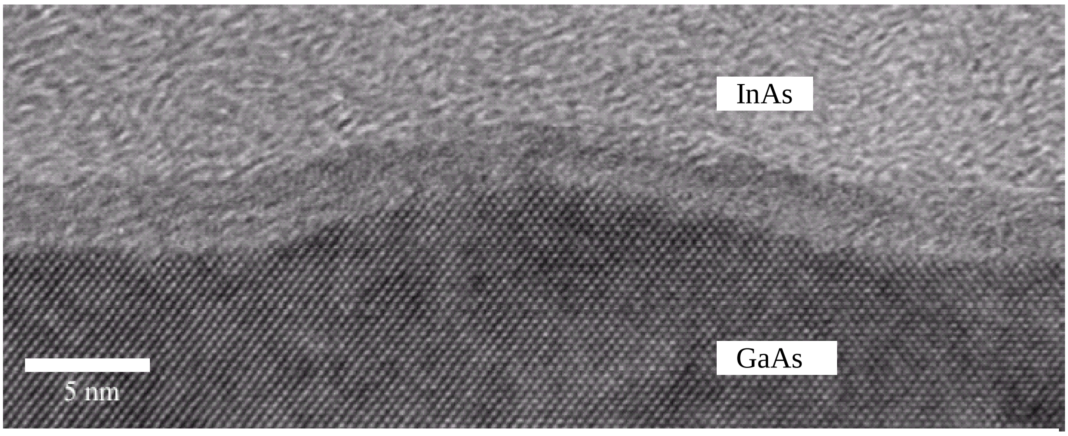

Figure 1.3.6.1.1 Transmission electron microscopy image of a single InAs quantum dot grown on GaAs. The dot's height is 36Å and its width is 24.5 nm (Sarney et al., 2002).

1.3.7 Heat Transfer in Compound Parabolic Concentrators

A one-dimensional thermal network illustrating the heat transfer in a CPC is shown in figure 1.3.7.1. This model adapted from Rabl (1985) neglects the effect of conduction through the frame from the absorber, through the aperture to reflector and the reflector to the absorber. The effect of conduction is minimal in comparison to other heat transfer mechanisms. Thermal losses from the aperture cover involves convection and radiation between each node. This is indicated by parallel resistances for convection and radiation.

A vorticity-based finite element model was developed for natural convection in compound parabolic concentrators (Abdel-Khalik and Randall, 1978). Their model assumed that the receiver and the cover plates were isothermal surfaces. A "Conduction Nusselt Number" was defined under no flow conditions, and a "Critical Rayleigh Number" was obtained by extrapolating convective Nusselt numbers to conduction limits. The variation of the ratio of Nusselt number to the conduction Nusselt number and the ratio of Rayleigh number to the critical Rayleigh number were given for five different concentration ratios. It was reported that for full and truncated CPCs the Rayleigh number varies as $2.0*10^3 \leq Ra \leq 1.3*10^6$ for the concentration ratio $2 \leq C \leq 10$ for a 5 cm deep CPC with T_s=200°C and T_l=25°C (Abdel-Khalik and Randall, 1978). 200 triangular elements of 121 nodes were used for their calculations.

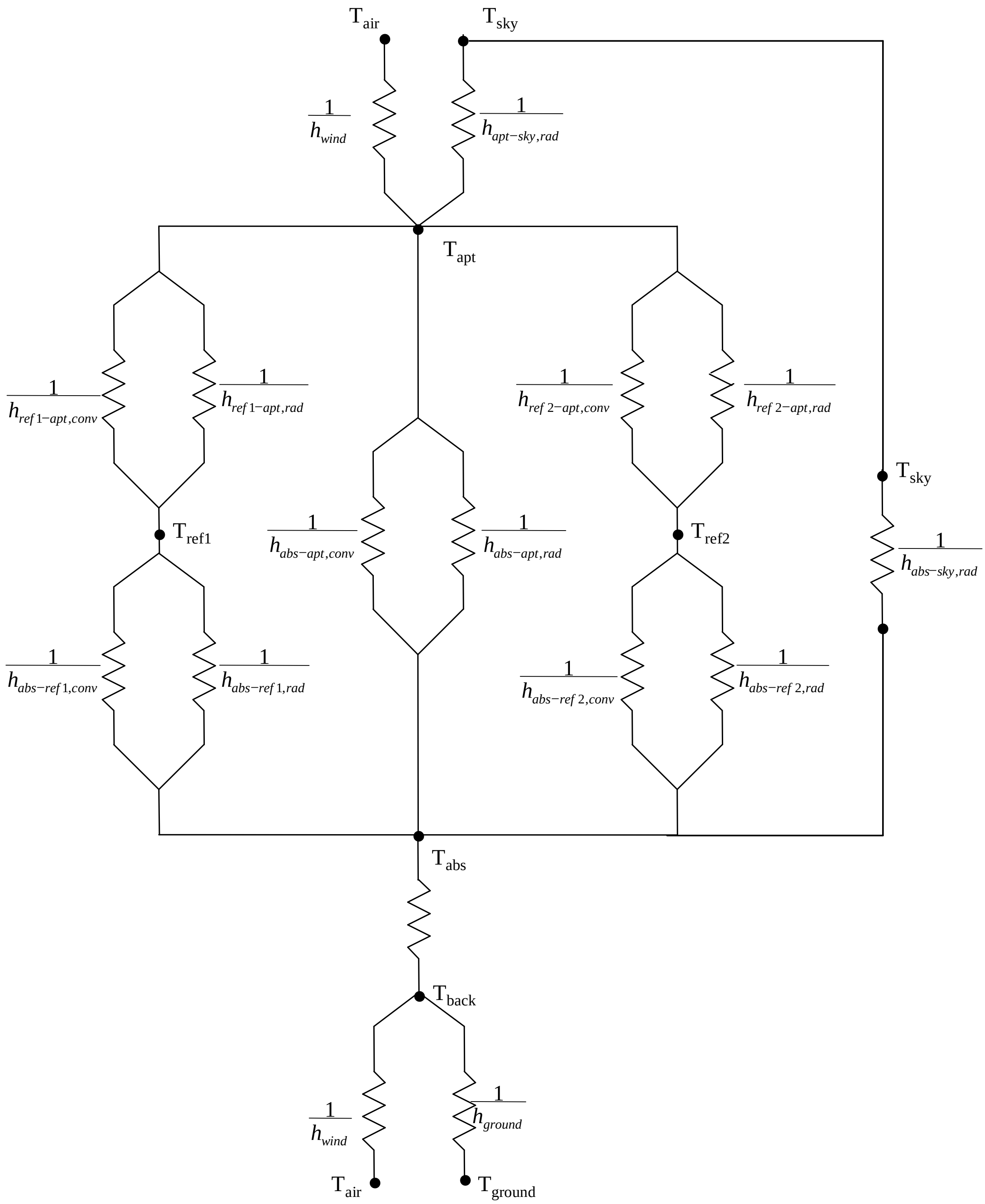

Figure 1.3.7.1 Thermal network for asymmetric compound parabolic concentrator (Adapted from Rabl, 1985).

Several authors have carried out computer simulations and experimentation into the thermal behaviour of tubular-absorber CPC's (Hsieh, 1981; Prapas et al., 1987a, 1987b; Chew et al. 1988, 1989; Eames and Norton, 1990, 1993a, 1993b, 1995, Eames et al., 2001). Hsieh (1981) did not considered either solar or long-wave radiation at the reflectors. Prapas et al., (1987a, 1987b) performed a thorough analysis taking into account energy absorbed at the reflector for different CPC's configuration.

The convective heat transfer coefficient employed in their model was (Hsieh, 1981)

$$h = 1.32\left(\frac{\Delta T}{2r}\right)^{0.25} \tag{1.3.7.6}$$

Prapas et al., (1987b), assumed unrealistically that the reflector, absorber and cover plate were all at constant temperatures. The temperature at the absorber, reflector and aperture cover were also non-uniform to an extent depending on the interaction between the flux intensity, thermal conductivity, and heat removal or loss.

A finite element based computer simulation and experimental investigation were undertaken by Chew et al., (1988, 1989) for heat transfer within a CPC. Triangular meshes were employed for their theoretical investigation. The reflector walls of the cavity were constituted to be adiabatic boundaries, this is not realistic due to longitudinal conduction across the reflector. The flow pattern in tall cavities tends to be of the unicellular type while when the cavity height is truncated to one third of the original cavity height, the flow pattern becomes a strong function of the tilt angle. For their experimental investigation Chew et al., (1988) used a 1m long polystyrene block whose internal profile was lined with aluminium foil to ensure that realistic long-wave thermal radiation properties prevailed. The absorber was simulated by a 32mm diameter copper cylinder, enclosing an electrical heating element. Ten thermocouples were used to monitor the temperature variations both circumferentially and axially. The temperature at the water cooled copper aperture cover was monitored by six thermocouples and several other thermocouples were used to measure the temperature along the profile of the CPC reflector and at the polystyrene end walls of the test section. The heat transfer correlation determined by Chew et al., (1988) was

$$Nu_H = 0.44\left(\frac{H}{W}\right)^{\frac{1}{6.5}}\left(Gr_H \bullet \mathrm{Pr}\right)^{\frac{1}{4}} \tag{1.3.7.7}$$

for $5\times10^4 < [Gr_H \bullet Pr] < 3\times10^7$,where W is the half-width of the flat top of the cavity.

A good agreement was reported between the analytical predictions (Chew et al. 1989) and their experimental investigation (Chew et al. 1988). The limitation of the experimental investigation was that only vertical orientations of the collector cavity were considered, these rarely ensue in reality. The numerical simulations at higher Grashof numbers in the vertical orientation gave results that contradict symmetry conditions. There were no energy loss or gain at the reflector and conduction across the aperture cover and around the absorber were omitted. These shortcomings were avoided by Eames and Norton, (1993a, 1993b) in their theoretical and experimental investigations. Detailed parametric analysis of heat transfer in CPCs used a ‘unified model’ for optical and thermophysical behaviour (Eames and Norton, 1993b). In a two-dimensional steady-state finite element analysis, no-slip boundary conditions were used for the fluid i.e., both velocity components were zero at the surface of the absorber, reflector and aperture cover. The predicted thermofluid behaviour of 60°, 30° and 45° acceptance half-angle CPCs were predicted for 0, 30 and 45° inclinations. A bicellular flow profile was reported for 0, 15 and 30° inclination angles for the 60° acceptance half-angle CPC as shown in figure 1.3.7.2. The average Nusselt number and Grashof number were calculated and a correlation was reported for both boundary conditions.

Theoretically calculated isothermal plots and velocity vector diagrams for different acceptance half angles showed that unicellular flow developed for lower acceptance half angles much faster compared to higher acceptance half angle CPCs. For a 60° acceptance half-angle CPC, a Grashof number was reported as 3.1×10^{6}. The predicted variation of Nusselt number around the enclosure of a 60° acceptance half-angle CPC was given at different collector inclinations. “Average Nusselt numbers” were defined for both unicellular and bicellular flow for different acceptance half-angle CPCs.

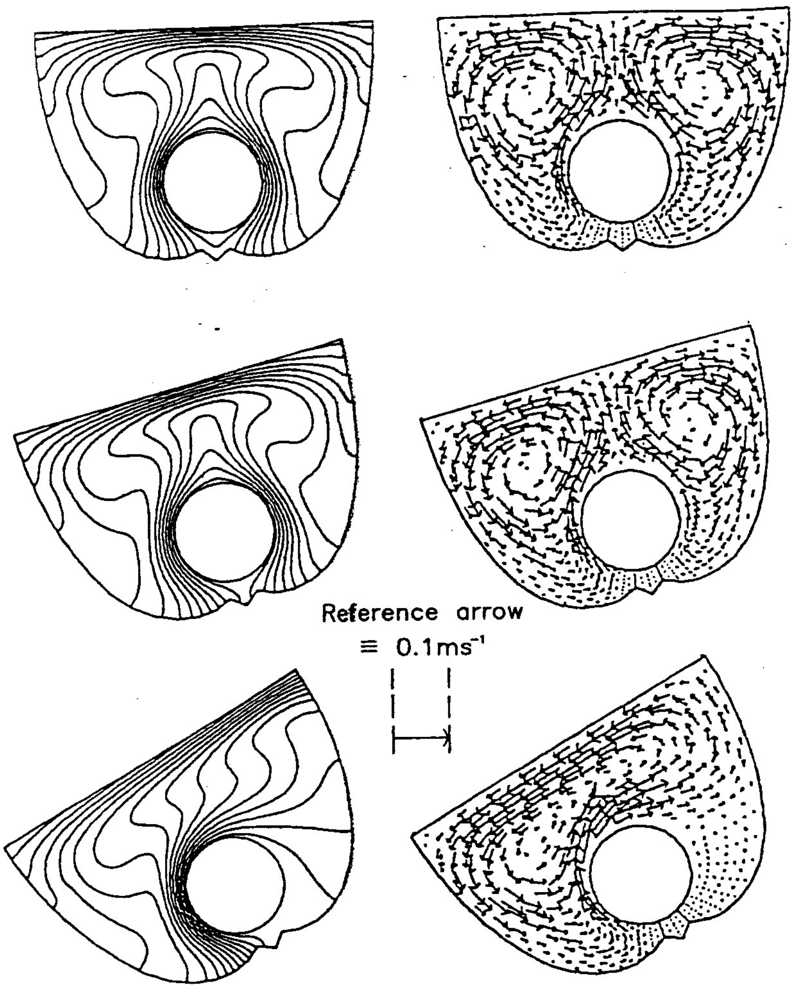

Figure 1.3.7.2 The theoretically calculated isothermal plots and velocity vector diagrams for a 60° acceptance half angle CPC inclined at 0, 15, and 30° to the horizontal (Eames and Norton, 1993b).

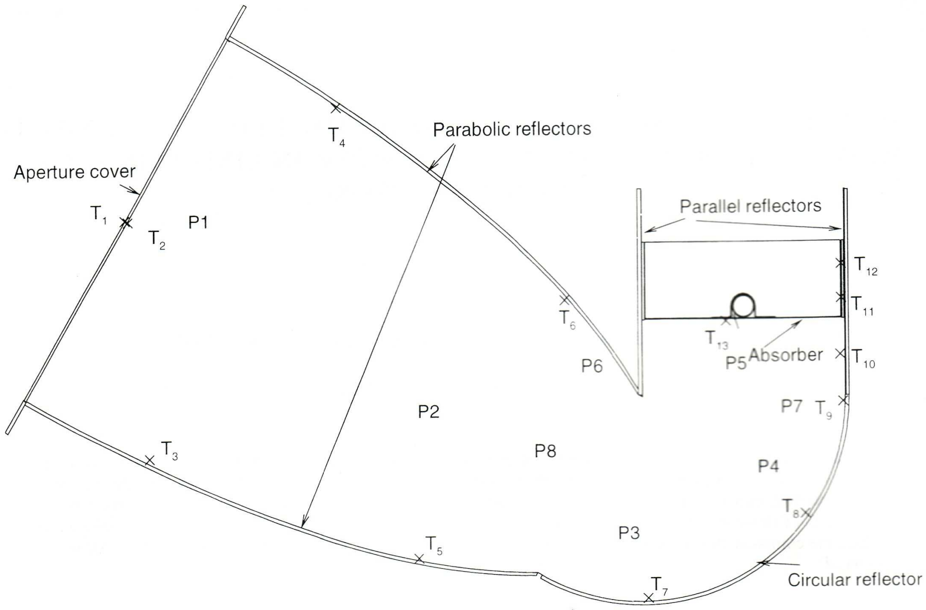

Figure 1.3.7.3 Schematic diagram of the 30° acceptance half-angle CPC augmented with a reverse flat plate absorber and the locations of thermocouples employed to verify the comprehensive unified model (Eames et al., 2001).

A theoretical model and an experimental investigation into the variation of angle of inclination on the performance of low-concentration-ratio compound parabolic concentrating solar collectors with tubular absorber was reported by Kothdiwala et al., (1995). This model was restricted to concentration ratios of less than five. The model assumed that the reflector surface is free from imperfections and that the aperture, receiver and reflector have a uniform temperature distribution.

A “Comprehensive unified” model for optics and heat transfer and its experimental validation for line-axis solar energy systems was reported by Eames et al., (2001). The experimental tests were conducted on a reverse flat plate collector augmented with a full 30° acceptance half-angle compound parabolic concentrator as shown in figure 1.3.7.3. The Eames et al., (2001) experimental investigation used a 4 mm glass aperture cover and parallel, circular and parabolic reflectors incorporated as shown in figure 1.3.7.3. Twelve thermocouples were used to measure the temperature at different location on the reflector and absorber. A large insulated hot water store with a thermostatically-controlled heater provided flow through the absorber at a range of constant temperatures. A pump provided a constant volume flow rate through the system and a flow meter located in the pipe circuit at a sufficient distance from the pump, valves and bends determined the volume flow rate. Temperatures predicted from the ‘comprehensive unified’ model (Eames et al., 2001) were within 2° of those measured experimentally as shown in table 1.3.7.1.

Thermocouple location	Asymmetric inverted CPC with 75 mm parallel walled reflector section			Asymmetric inverted CPC with 75 mm parallel walled reflector section			Asymmetric inverted CPC with 125 mm parallel walled reflector section			Asymmetric inverted CPC with 75 mm parallel walled reflector section		
	Experiment	Prediction	Difference	Experiment	Prediction	Difference	Experiment	Prediction	Difference	Experiment	Predicted	Difference
T_{inlet}	37.0			23.72			29.22			Fluid recirculation in absorber pipe $T_{\text{inlet}} = T_{\text{outlet}}$		
T_{outlet}	39.9			31.80			35.71					
T_{FA}	38.5	Set 38.5	–	27.8	Set 27.8	–	32.5	Set 32.5	–	16.0	Set 16.0	–
T_{amb}	11.1	Set 11.1	–	10.8	Set 10.8	–	12.8	Set 12.8	–	13.1	Set 13.1	–
T_1	29.3	29.7	0.4	28.6	29.2	0.6	30.2	31.2	1.0	33.6	33.3	−0.3
T_2	30.0	30.1	0.1	29.3	29.5	0.3	31.0	31.6	0.6	34.6	33.7	−0.9
T_3	29.3	28.6	−0.7	28.3	28.0	−0.3	31.4	30.3	−1.1	31.9	32.4	0.5
T_4	27.2	28.3	1.1	26.7	27.7	1.0	29.0	29.4	0.4	29.3	30.6	1.3
T_5	28.1	27.4	−0.7	27.1	26.2	−0.9	30.1	29.2	−0.9	30.7	30.9	0.2
T_6	28.5	27.9	−0.6	27.1	26.7	−0.4	29.7	30.1	0.4	33.7	33.7	0.0
T_7	29.5	29.7	0.2	27.3	28.9	1.6	31.2	30.2	−1.0	34.4	33.2	−1.2
T_8	30.1	31.1	1.0	29.8	30.1	0.3	31.9	32.0	0.1	35.9	36.4	0.5
T_9	27.9	28.9	1.0	27.3	27.6	0.3	29.1	29.4	0.3	36.1	37.6	1.5
T_{10}	28.2	28.9	0.7	27.3	27.3	0.0	29.0	29.2	0.2	38.9	40.0	1.1
T_{11}	26.0	26.2	0.2	25.3	24.9	−0.4	28.2	30.2	2.00	35.2	36.3	1.1
T_{12}	23.8	22.6	−1.2	23.4	21.9	−1.5	28.3	29.5	1.2	31.6	30.8	−0.8
T_{13}	57.4	56.9	0.5	47.8	48.4	0.6	52.2	52.4	0.2	113.8	113.5	0–3

Table 1.3.7.1 Experimental and predicted temperatures of asymmetric inverted CPC with 75 mm and 125 mm parallel walled reflector section for validation of comprehensive unified model (Eames et.al., 2001). The thermocouples were located as illustrated in figure 1.3.7.3.

1.3.8 Nusselt Number Correlation for a CPC

Nusselt number is the dimensionless temperature gradient at a surface. It provides a measure of the convection heat transfer occurring at that surface and is defined as (Incropera and DeWitt, 1996)

$$Nu = \frac{hL}{k_f} \equiv \left. \frac{\partial T^*}{\partial y^*} \right|_{y^* = 0} \tag{1.3.8.1}$$

Several convective heat transfer correlations for CPC's have been reported in the literature:

- for CPC-type cavities with a tubular absorber (Chew et al., 1988)

$$Nu = a\left(\tfrac{H}{W_2}\right)^b (Gr_H , \Pr)^c \tag{1.3.8.2}$$

- for a tube enclosed eccentrically and collinearly within a larger tube or CPC (Prapas et al., 1987a)

$$Nu_{(r_{equ}-r_i)} = F_{ecc}\left(c\frac{r_{equ}}{r_i} - a\right) Gr^b_{(r_{equ}-r_i)} \tag{1.3.8.3}$$

- for CPC-type cavities with flat-plate absorber (Tatara and Thodos, 1985)

$$Nu_H = a(Ra_H)^c \tag{1.3.8.4}$$

- incorporating angular inclination on the internal convective heat transfer within a CPC cavity (Eames and Norton, 1993b)

$$Nu = \frac{1}{(a+b\cos(\theta-45))} \times \left(\frac{H}{W_2}\right)^n Gr^{(c+d\cos(\theta-45))} \tag{1.3.8.5}$$

1.4 Photovoltaic Solar Energy Utilisation

The photovoltaic effect was discovered by Edmund Becquerel while experimenting with an electrolytic cell made up of two metal electrodes (Becquerel, 1839). He noted that a voltage appeared when one of two identical electrodes in a weak conducting solution were illuminated. The discovery of the p-n junction enabled the production of the single-crystal germanium solar cell at the Bell Laboratory (Chapin et al., 1954). With the advent of the space program, photovoltaics made from semiconductor-grade silicon quickly become the source of power for satellites.

When a uniform p-type Silicon sample is metallurgically joined to a uniform n-type sample, a p-n junction is produced and the positive and negative electrical charges redistribute, establishing internal electric fields that determine the properties of the semiconductor diode. At the instant of time of junction formation, the concentration of electrons is much larger on the n side than on the p side and the hole concentrations which is larger on the p-side than on the n-side. This difference in carrier concentrations sets up an initial diffusion current i.e. electrons flow from the n region into the p region, and holes flow from the p region into the n region. This flow of charge creates a region near the junction that is depleted of majority carriers that is, of electrons on the n side and holes on the p side. The fixed donor and acceptor impurity ions in this depletion region are no longer balanced by the free charges that were once there. As a result an internal electric field builds up with a direction that opposes a further flow of electrons from the n region and holes from the p region. The magnitude of the field is such that it exactly balances the further flow of majority carriers by diffusion. The region around the junction is depleted of majority carriers, and a space-charge layer forms in the region of high electric fields. In presence of solar photons, due to the creation of electron holes pairs, the equilibrium conditions of the p-n junction are disturbed. Minority carriers (i.e. electrons in the p material and holes in the n materials) are created in sufficient quantities to lower the potential energy barrier at the junction, allowing a current to flow and establishing a potential difference across the external terminals. Only some parts of the solar spectrum are converted to electricity as shown in figure 1.4.1 and figure 1.4.2.

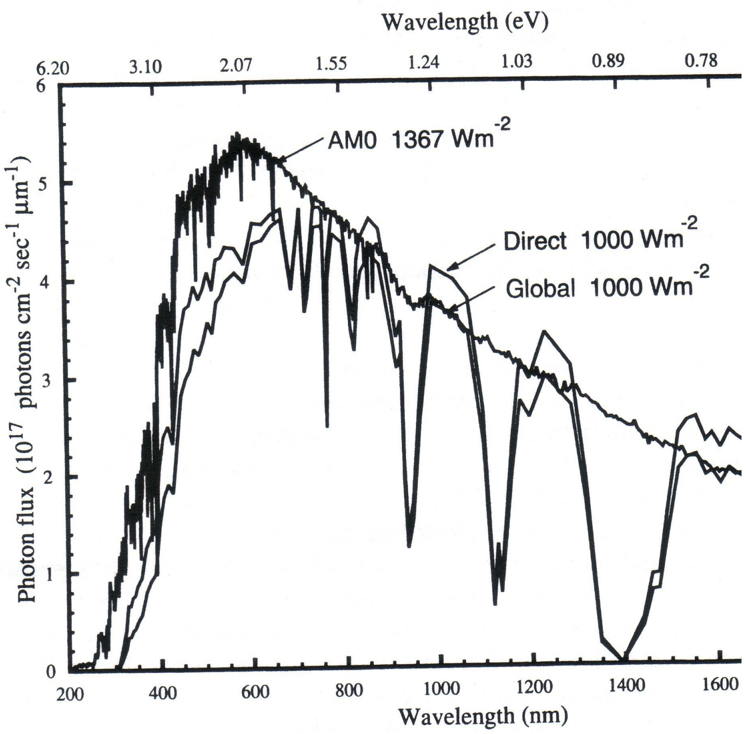

Figure 1.4.1 Direct and terrestial component of solar energy spectrum at AM0 and standard AM 1.5 (Duffie and Beckman, 1991).

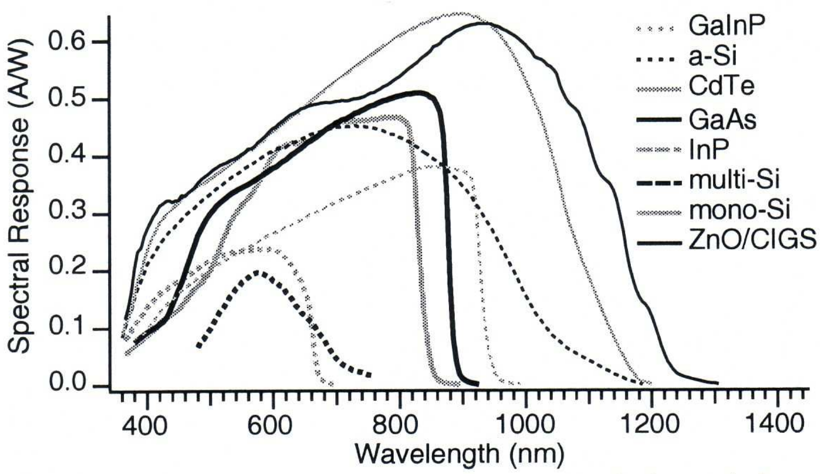

Figure 1.4.2 The spectral response characteristics of different types of solar cell (Field, 1997).

Photovoltaic efficiency is defined as the ratio of output electrical energy to incident solar energy on the photovoltaic surface. The theoretical upper limit of solar cell efficiency depends on the type and fabrication of the solar cell. A quantum-well solar cell under isotropic black-body radiation would achieve an optimal efficiency of 54.5% (Honsberg et al., 1997) whereas for homojunction solar cells the limiting efficiency is 30% (Shockley and Queisser, 1961). A measured 24% module efficiency for a multicrystalline silicon solar cell have been reported by Green (1997a, 1997b). The energy absorbed by the solar cell not converted into electricity is manifest as heat.

1.5 Different Photovoltaic Solar Cell Technologies

Photovoltaic research and development aims to (Green, 1982):

- improve collection of incident photon flux by minimizing front contact area
- improve collection of carriers by incorporating back surface electric fields to reflect minority carriers

- minimise resistive losses
- minimise recombination losses
- minimise solar cell temperature and thus output electrical efficiency.

1.5.1 Silicon Solar Cells

The earliest silicon cells benefited from the slow solidification process used in silicon microelectronics manufacturing causing a serendipitous distribution of p-type (boron) and n-type (phosphorous) impurities in the silicon (Green, 2000). The development of bifacial solar cells improved the fraction of current transferred from the rear to the front and increased the magnitude of shunt resistances improving solar cell characteristics (Honsberg et al., 1997).

1.5.1.1 Single-Crystal Silicon Cells

In a typical n-p or p-n junction solar cell wafer, p-type single-crystal silicon is diffused by phosphorus atoms onto the top surface. Figure 1.5.1.1.1 shows the construction of a typical n-on-p type solar cell. The development of single crystal silicon solar cell is shown in figure 1.5.1.1.2. The metal/insulator/n-type/p-type (MINP) and passivated-emitter solar cell (PESC) design by Kazmerski (1997) as shown in figure 1.5.1.1.2(b) & 1.5.1.1.2(c) has reported an efficiency of 21%. These cells are designed specially for high V_{oc} and have been fabricated into large operational areas. For a single crystal Silicon "dot-contact" (contacts are through the back, so that no light is obscured by a front contact) an efficiency of 22% has been reported (Weber et al., 1997).

Bifacial silicon cells as shown in the figure 1.5.1.1.2(e) convert sunlight incident on both device surfaces. These cells have the advantage of utilising reflected light either from the surroundings or from static concentrators. The complex manufacturing process required means these solar cells are not used widely (Kazmerski, 1997). Despite the predominance of single junction solar cells, solar cells can be made as triode or transistor structure solar cells (Pritchard et al., 1997).

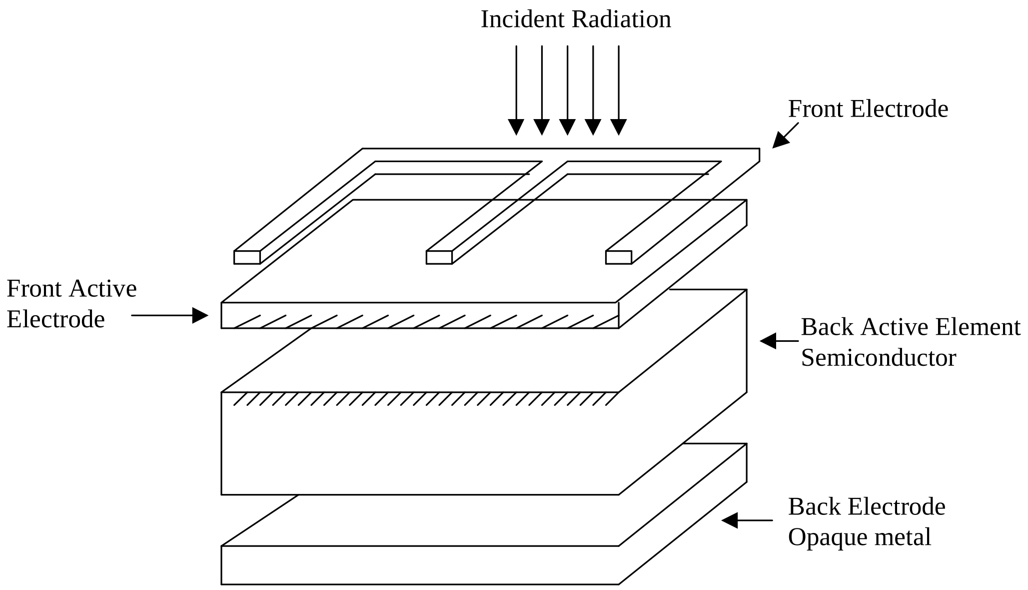

Figure 1.5.1.1.1 Cross section of solar cell construction (Kazmerski, 1997).

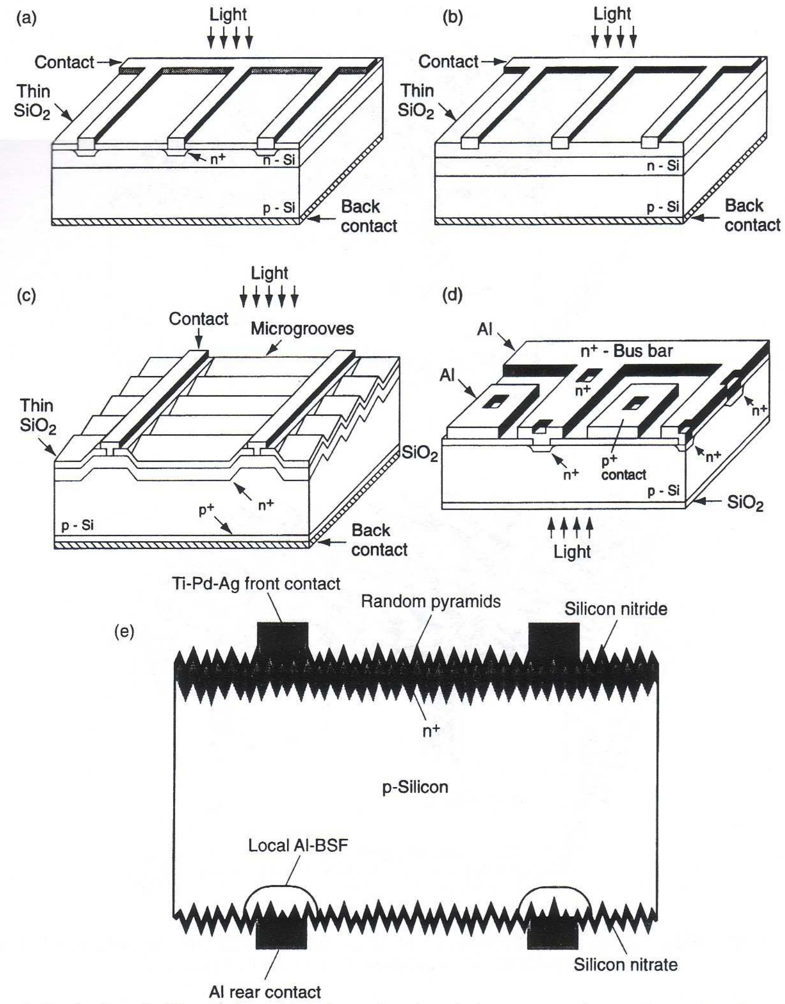

Figure 1.5.1.1.2 Evolution of silicon solar cell designs, showing device cross-sections: (a) p-n junction; (b) metal-insulator, n-type cell (MINP); (c) passivated-emitter solar cell (PESC); (d) point-contact cell; (e) bifacial solar cell (Kazmerski, 1997).

1.5.1.2 Polycrystalline, Multicrystalline and Thin-Silicon cells

Grain boundaries, twins, dislocations, voids and segregated species impurities are all potential sources of electrical shunts and shorts that may be avoided using single crystal Silicon solar cells (Kazmerski, 1997). A major cost factor for Silicon solar cells is the production of high purity and high perfection Silicon wafers. Lower energy use and the utilisation of lower purity feedstock Silicon reduces production cost (Kazmerski, 1997) but sacrifices crystalline order and device efficiency.

Polycrystalline cells have been treated with active gases and inorganic materials to minimise the effect of active defects and the surface boundaries (Kazmerski, 1997) although for lower efficiency devices these techniques give only a small performance improvement. Thin film Silicon solar cells can provide better materials utilisation. Early attempts to produce thin film Silicon cells resulted in devices with a very low efficiency, typically of 5%. With technological improvement using vacuum deposition and chemical vapour deposition techniques thin film Silicon solar cells have been produced with an efficiency of 19% (Brendel, 1997).

1.5.2 Indium Tin Oxide Solar Cells

Indium tin oxide (ITO) solar cells are hetero-junction types with p-type silicon doped with tin oxide or indium oxide. Both the later are n-type semiconductor materials and are transparent to the visible region of the solar spectrum but are good conductors of electricity. Tin oxide can be deposited easily onto glass or other substrates by spraying tin chloride in water onto an heated substrate (Archer and Hill, 2001).

1.5.3 Metal-Semiconductor Junctions Solar Cells

Another type of junction that can be used in a solar cell is the Schottky barrier (Komp, 1995) or metal to semiconductor junction. This junction is produced when a low work-function metal like aluminium is deposited onto a p-type semiconductor or a high work-function metal like gold is deposited onto a n-type semiconductor (Komp, 1995). Metal-insulator-semiconductor junctions can be formed if an extremely thin insulating oxide layer is placed between the metal and the semiconductor (Hovel, 1980). Schmidt et al., (1994) predicted that an efficiency of 10% can be achieved for metal-semiconductor junction solar cells.

1.5.4 Photoelectrochemical Solar Cells

In a photoelectrochemical solar cell molten silicon is poured through screens to make small droplets that solidify to form silicon electrodes as they fall through a “shot tower” (Komp, 1995). The simplified fabrication steps and the ability of the device to produce hydrogen as well as electricity created an interest in this technology as a possible component of a future hydrogen economy. In such a solar cell, the liquid induces a barrier in the semiconductor same way as does a metal. The liquid contains a species know as redox couple with two charge states (Gordon, 2001). The species changes from an oxidised state to a reduced state if it accepts an electron, or undergoes the opposite process of oxidation if it gives up an electron. Light is absorbed in the semiconductor creating an electron-hole pair as it does in the single crystal Si solar cell. For this type of solar cells, 11.5 % electrical efficiency has been reported (Gordon, 2001).

1.5.5 Cadmium Sulphide / Cadmium Telluride Solar Cells

Hetero-junction cadmium sulphide/cadmium telluride solar cells are produced by dipping a cadmium sulphide layer into a copper chloride solution (Meyers and Liu, 1988; Ponpon, 1985). The main disadvantage of these types of solar cells is that the junctions react with chemicals and moisture in air and degrade rapidly. Silkscreen printing and spray coating process produce thin film CdTe cells with efficiencies of around 13% (Komp, 1995). Atomic layer epitaxy using close-spaced sublimation has produced Cds/CdTe solar cells successfully with an efficiency of almost 16% (Granata et al., 1996).

1.5.6 III-V Semiconductor Solar Cells

III-V semiconductors such as GaAs, GaAlAs, GaInAsP, InAs, InSb and InP have received particular attention as photovoltaic materials because of the spectral matching of their band gaps to solar radiation (Yeh et al., 1996; Takahashi et al., 1998). A 28% efficient solar cell was reported using gallium arsenide/gallium antimonide. The main disadvantages of these semiconductors are that these are rare materials with consequently very high prices. A potential application for III-V solar cells in the future is terrestrial solar concentrator systems for large-scale electricity production (Alferov, 2000) operating at high illumination intensities, equivalent to 500 to 1000 suns (Dimroth et al., 2000). At high concentration levels, III-V semiconductor solar cells can reach efficiencies higher than 33% (Green et al., 2000) and the degradation of the solar cell performance at high working temperatures is much smaller than compared to Silicon solar cells (Dimroth et al., 2000).

1.5.7 CIS Solar Cell

$CuInSe_2$(CIS) has become one of the leading candidates for economic polycrystalline solar cell structures (Archer and Hill, 2001). CIS film formation can be made using thermal evaporation in vacuum, electrodeposition, chemical dipping or chemical vapour deposition method (Fernanez et al., 1996). The electrical efficiency of CIS based solar cell have shown electrical conversion efficiency of 8% and do not show evidence of any degradation (Fernanez et al., 1996).

1.5.8 **Single-Junction Approaches**

Most solar cells exhibit higher efficiencies under increased solar irradiance. However reflection or refraction loses in the concentrator can reduce available radiation by as much as 10%. GaAs-based solar cells have been reported which minimise high surface recombination to give an efficiency of 21% at AM1.5 (Kazmerski, 1997). Metal-organic chemical vapour deposition methods, molecular-beam epoxy (Chow, 1991) and cleavage of the epitaxial film technology (Fan et al., 1984) have been used to form single junction solar cells. Single-junction solar cell efficiencies are shown in table 1.5.7.1.

		Absorber band gap (eV)	Efficiency (%)	Reference
Cell Structures	CdTe (homojunction)	1.50	10.7	Barbe et al., (1982)
	InP (homojunction)	1.34	21.9	Keavney et al., (1990)
	GaAs/GaInP	1.42	25.7	Kurtz et al., (1990)
	Si (homojunction)	1.12	24.0	Zhao et al., (1995)
	Cu(In,Ga)Se_2/CdS	Graded	17.7	Tuttle et al., (1996)
	CdTe/CdS	1.45	16	Ohyama et al., (1997)

Table 1.5.7.1 Single-junction solar cell efficiencies.

1.5.9 **Electroplated Solar Cells**

Direct band gap semiconductors absorb light to create the charge carrier inside the material and thus a thin size of solar cell is implied. Being a passivated grain boundary and not acting as a recombination centre, the crystal grain can be even smaller than that formed for thin film solar cells using electroplating methods with cuprous oxide, zinc phosphide and cadmium telluride (Komp, 1995). Schottky barrier solar cells can be made using the thin Cuprous oxide layer formed and lying under the copper. These cells have displayed an efficiency of 2% although theoretical studies indicate that an efficiency of 13% is possible using these types of materials (Green, 2000).

1.5.10 **Organic Semiconductor Solar Cells**

Organic materials have been used as photosensitizers and directly as the semiconductor element in a solar cell (Kearns and Calvin, 1958; Borsenberger and Wiss, 1993; Halls et al., 1995; Yu et al., 1995; Halls et al., 1999). Dyes coating tiny silver halide crystals can absorb the visible region of the solar spectrum and convert it into electrical power. Photoelctrochemical cells which can produce both hydrogen and electricity can be made by dying titanium dioxide-coated electrodes with an organic dye phthalocyanine to render them absorbent to the visible sunlight that titanium dioxide normally reflects (Archer and Hill, 2001). Dye-densitised inorganic oxide photoclectrochemical cells have been made by coating titanium dioxide with ruthenium containing organic dyes (Greenham et al., 1996). These dyes bind extremely well to colloidal titanium oxide allowing a thin and highly absorbing film to be formed on glass. Conductively coated glass can thus be used as a window electrode in a liquid cell. An opaque platinum coated counter electrode forms the back contact. Such solar cells have been reported to have an efficiency of 12% (Halls et al., 1999).

1.5.11 Cascade Solar Cells

The cascade solar cell, first reported in 1953 (Komp, 1995), is a stack of different solar cells, each of which absorbs a part of the solar spectrum and passes the rest of the light for absorption at the next layer. Silicon solar cells have the largest band gap and the shortest cut-off wavelength and transmit most light redder than this wavelength. This light is absorbed by materials with narrower band gaps placed behind the first cell. A single narrow band gap material can be placed at the back of these cells to absorb the infrared radiation. The cascade cell has an output voltage that is the sum of the individual cells, but the output current of the device is less than that of narrow band gap solar cells, however the overall efficiency ends up much higher. Gallium arsenide and gallium aluminium/gallinium arsenide cascade solar cells have been reported with an effective output efficiency of over 33% (Komp, 1995).

1.6 Photovoltaic Applications in Building Integration

Approximately 25-30% (Sick and Erge, 1996) of energy consumed in the building sector for industrialised countries is in the form of electricity. Photovoltaics can be integrated on virtually every conceivable structure from bus shelters to high rise buildings. The potential for PV in buildings depends on solar radiation availability on building surfaces, economical viability, architectural and structural compatibility, institutional restrictions and electricity grid stability (Watt et al., 1998a).

1.6.1 International Building Integrated Photovoltaics Market

Photovoltaics as a part of the building envelope accounted for 20% of the rapidly growing world PV market in 1998-99 (Watt et al., 1999). The global annual production of photovoltaics has grown by about 18-20% per year over the last 20 years with increasing remote area applications (Lin and Carlson, 2000). With the support of the International Energy Agency, European Union and individual country programmes, the market is likely to continue to grow. The European Union has set a target of 1,000,000 rooftop and façade integrated PV systems by the year 2010 (Schoen, 2001). The US has planned a 1 million solar (PV and thermal) rooftop programme (Watt et al., 1999). Market projections have suggested that PV will become competitive with utility peak power around 2030-2040 (Butz, 1999; Hoffman, 1999). An average production market growth rate of $17\%yr^{-1}$ is predicted of which grid connected system growth could be on average 25%/yr. Almost $1GW_pyr^{-1}$ PV market growth (Butz, 1999) can be expected by the year 2010 as shown in figure 1.6.1.1. The main photovoltaic markets are shown in figure 1.6.1.2. In the

UK it was estimated that installed PV increased from 173 kW_p in 1992 to about 670 kW_p in 1998 as shown in figure 1.6.1.3 (ETSU, 1999).

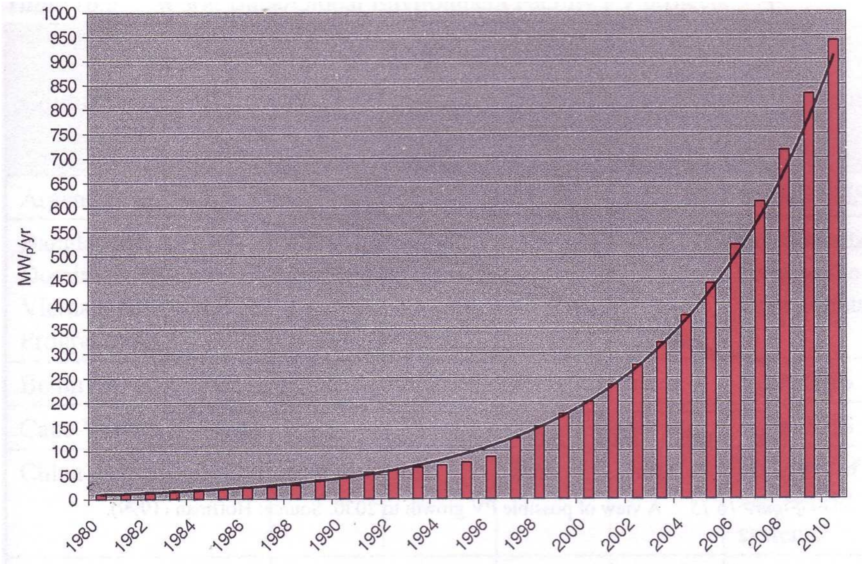

Figure 1.6.1.1 Past and projected future development of the worldwide PV for the years 1980 to 2010 (cells and modules together; Butz, 1999).

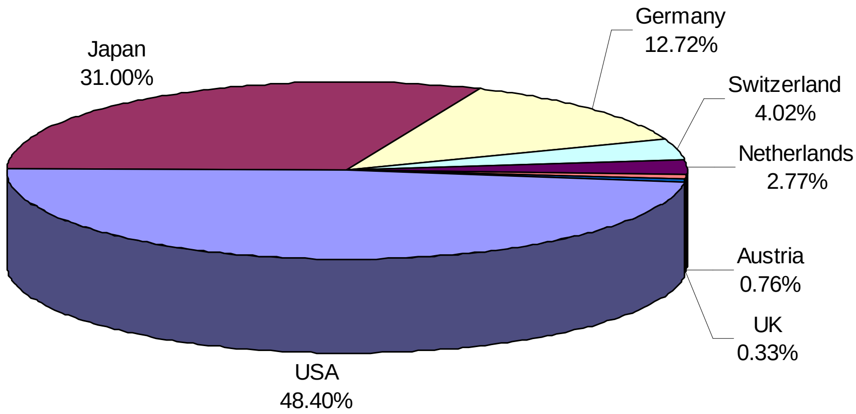

Figure 1.6.1.2 Country wise total Photovoltaic market capacity in the world (ETSU, 1998).

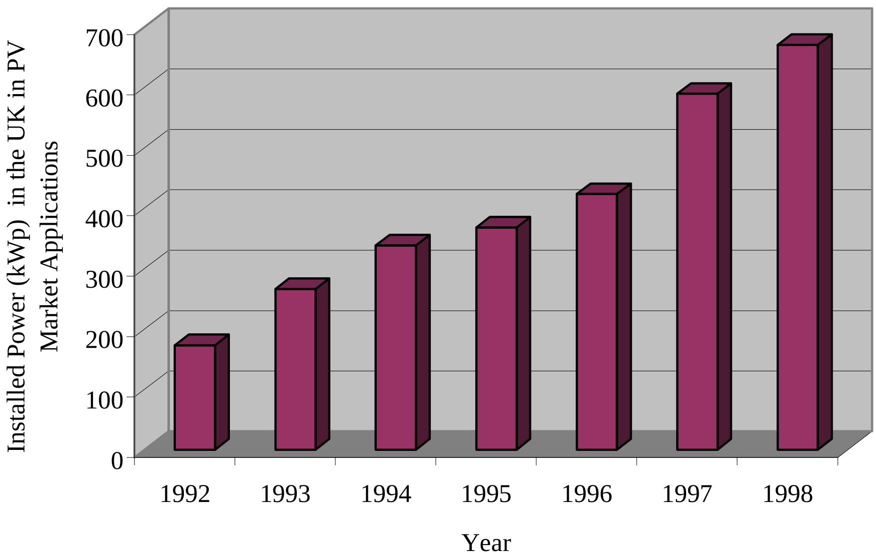

Figure 1.6.1.3 Cumulative total of UK installed power (kWp) in photovoltaic market applications (ETSU, 1999).

1.6.2 Different Building Integrated Photovoltaic Technology

Photovoltaic system can be incorporated into existing roofs, façades and curtain wall building elements dependent on the location (in relation to overshading) and design of the building. Building integrated photovoltaics (BIPV) can either be integrated into or replace an existing building element.

1.6.2.1 Building Rooftop Integrated Photovoltaic Systems

Most roof-mounted systems are retrofitted and hence are not fully integrated into the roof structure but are mounted onto existing roofs (Watt et al., 1999). Fully integrated BIPV roofing systems must perform the function of a standard roof and provide water tightness, drainage, and insulation. Ballast mounted or rack mounted roof system are shown in figure 1.6.2.1.1. PV systems can be mounted on a flat roof (figure 1.6.2.1.1 a) or a PV saw-tooth profile roof can be mounted as a ballast mounted panel with a clear glazed rear (figure 1.6.2.1.1 b).

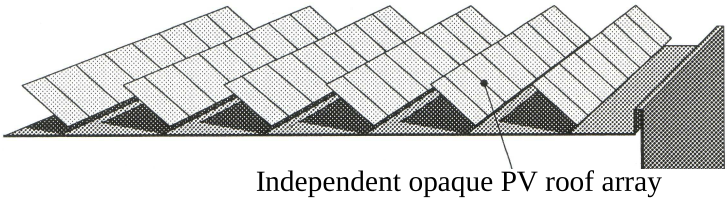

(a)

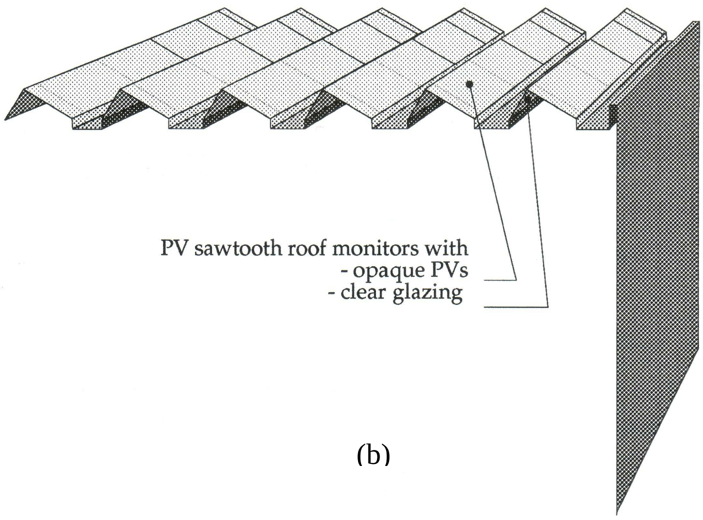

(b)

Figure 1.6.2.1.1 Building rooftop integrated photovoltaics: (a) frame mounted panel on a flat roof, (b) ballast mounted panels with clear glazed rear (Sick and Erge, 1996).

1.6.2.2 Building Wall and Façade Integrated Photovoltaics

Photovoltaic systems for building integration are shown in figure 1.6.2.2.1 to 1.6.2.2.3 integrated onto the building façade as (Sick and Erge, 1996)

- rainscreen overcladding
- pressure plate mullion / transom (stick) curtain wall systems
- structural glazing mullion / transom curtain wall systems
- panel curtain wall systems
- profiled metal cladding.

Two basic curtain wall framing system are pressure plate and structural silicone glazing. In pressure plate systems, the glazing unit is mechanically held from the front by a plate with an extended cover. Structural glazing glues some or all of the glazing edges to the framing systems. In pressure plate systems, the mullion cap depth must be kept to a minimum to avoid adverse shading of PV cells. Alternatively, the flush application of a structural silicone seal between PV glazing units eliminates shading effects but increases weather seal and durability problems for PV panel edges. A double wall envelope minimises sealing problems or allows heat capture from the PV modules. The PV glazing forms an external, unsealed layer with the inner layer forming a weathertight enclosure. Façade integration may require a sloped or 'saw-tooth' profile as shown in figure 1.6.2.2.3. Depending on the building design PV can be integrated in to a slopping wall or facade as shown in figure 1.6.2.2.3b. Issues for building integrated photovoltaics include:

- Structures must be capable of bearing photovoltaic modules.
- Overheating of PV elements due to weathertight seals (A sealed façade in Austria produced 4% less energy annually when compared to a rear ventilated system (Wilk, 1994), in warmer climates this loss may be higher).
- Design of forced and/or natural ventilation behind the PV elements. A temperature reduction of up to 20 K can be achieved by heat transfer to an airflow induced by buoyancy in a duct behind the PV component. This both increases the electrical output and reduces building heat gain (Brinkworth et al., 1997).
- A suitable aesthetic appearance is important particularly for prestige commercial curtain wall façades. Aesthetic considerations have led to the manufacture of coloured PV cells. The need to accommodate wiring in façades, which are often designed to appear frameless can also impact upon façade appearance (Watt et al., 1999).
- Glazed PV modules (c-Si and a-Si) and modules which are deposited onto a metal or other substrate (a-Si) require different approaches to fabric integration (Crick et al., 1998).
- Façades are shaded more frequently than roofs. Non-homogeneous shading of a PV façade will impact upon the electrical configuration, including the number of series and parallel strings, redundant interconnections and inverter sizing (Groehn and Barthels, 1994).

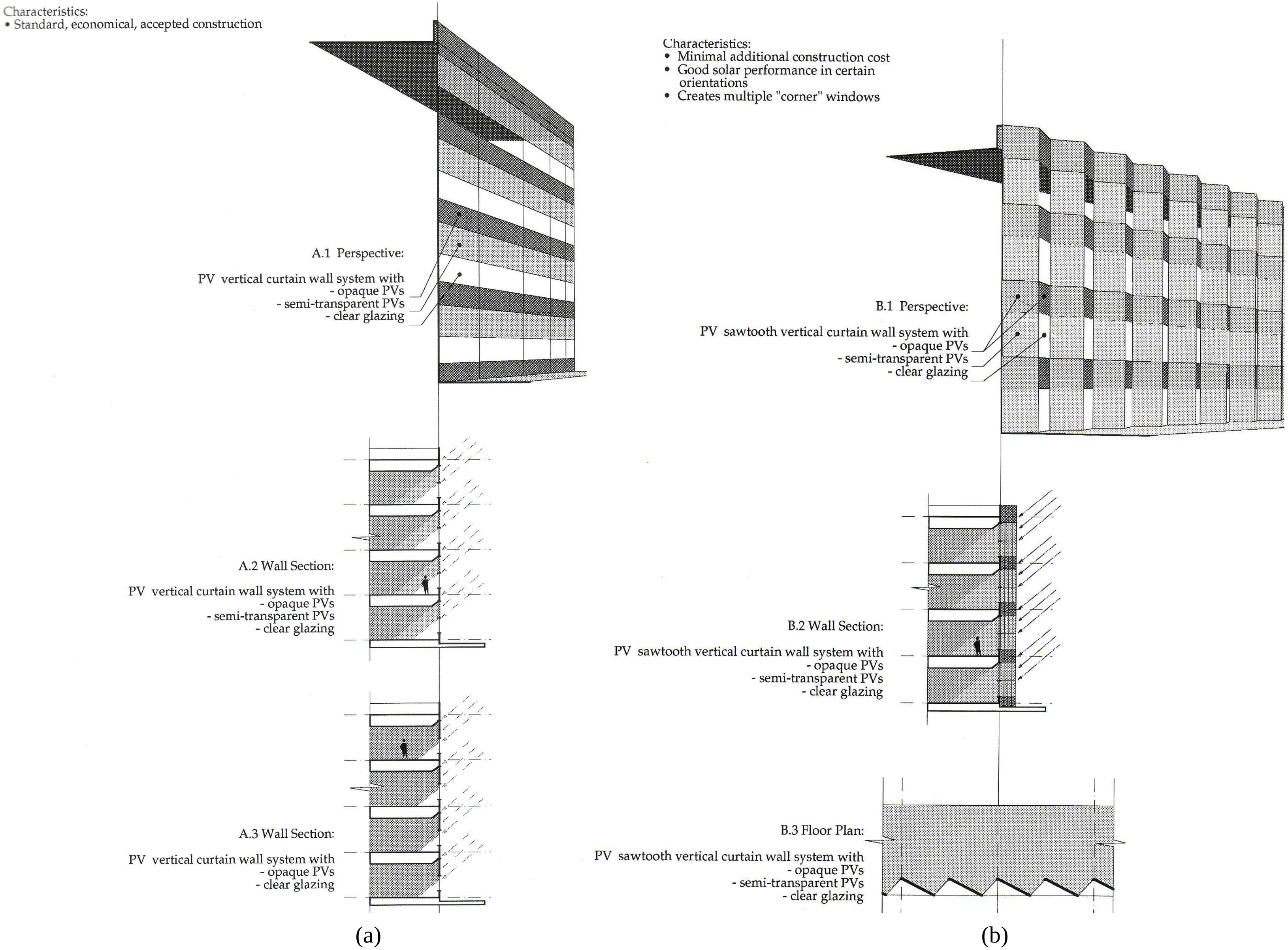

Figure 1.6.2.2.1 Applications of Photovoltaics onto building walls: (a) vertical curtain wall i.e. PV systems are integrated into the vertical wall with opaque PVs and semitransparent PVs, (b) sawtooth vertical curtain wall i.e. vertical curtain wall with opaque PVs or semi transparent PVs (Sick and Erge, 1996).

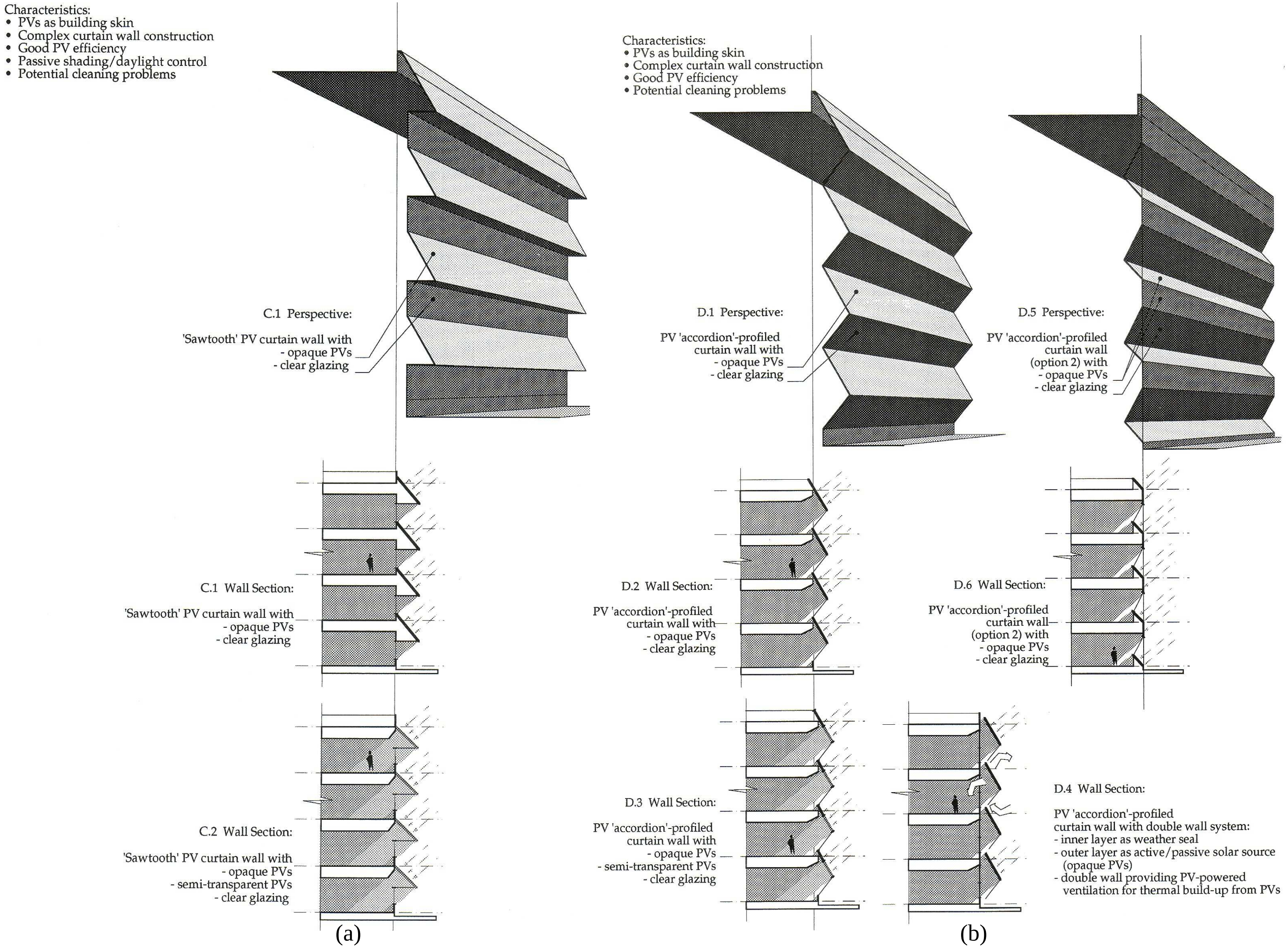

Figure 1.6.2.2.2 Applications of Photovoltaics onto building walls: (a) sawtooth curtain wall i.e. PV system are integrated into the vertical wall with opaque PVs (b) PV accordion curtain wall i.e. PV 'accordion' profiled curtain wall with with opaque PVs (Sick and Erge, 1996).

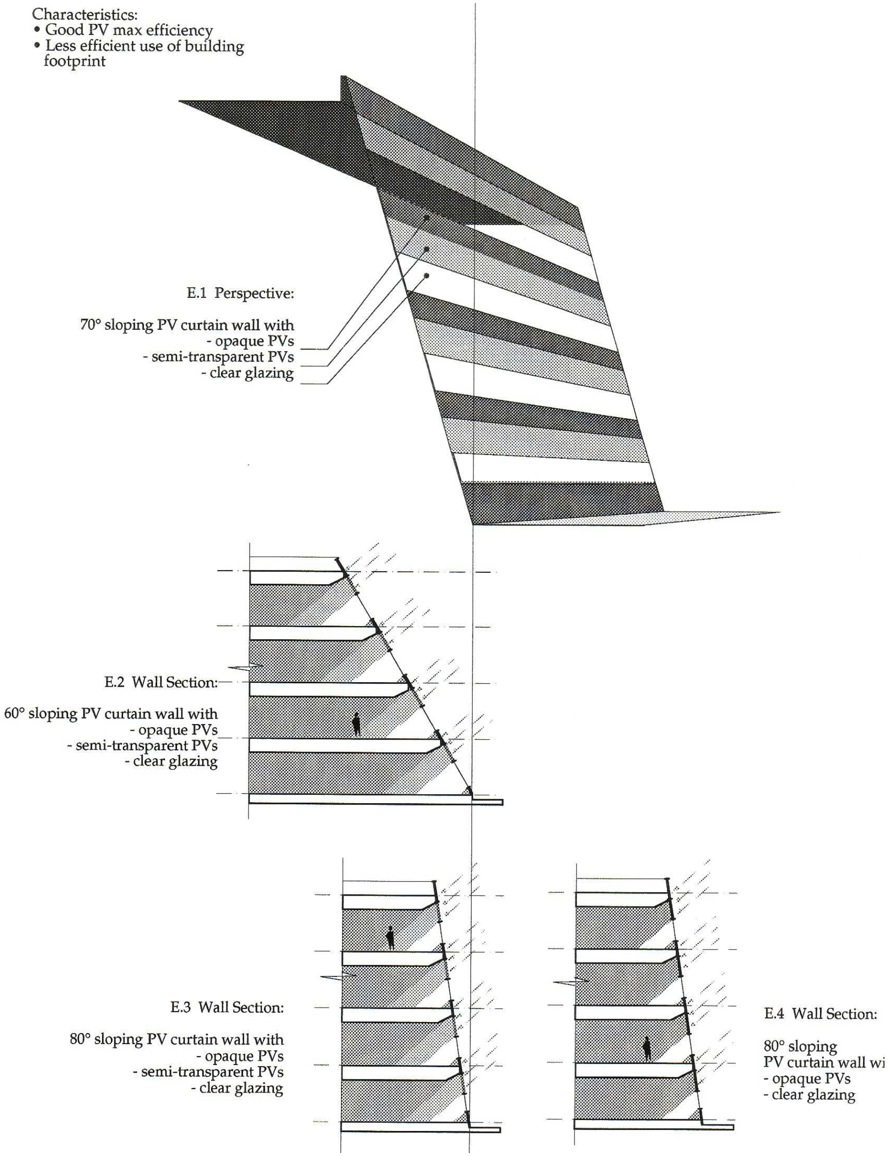

(a)

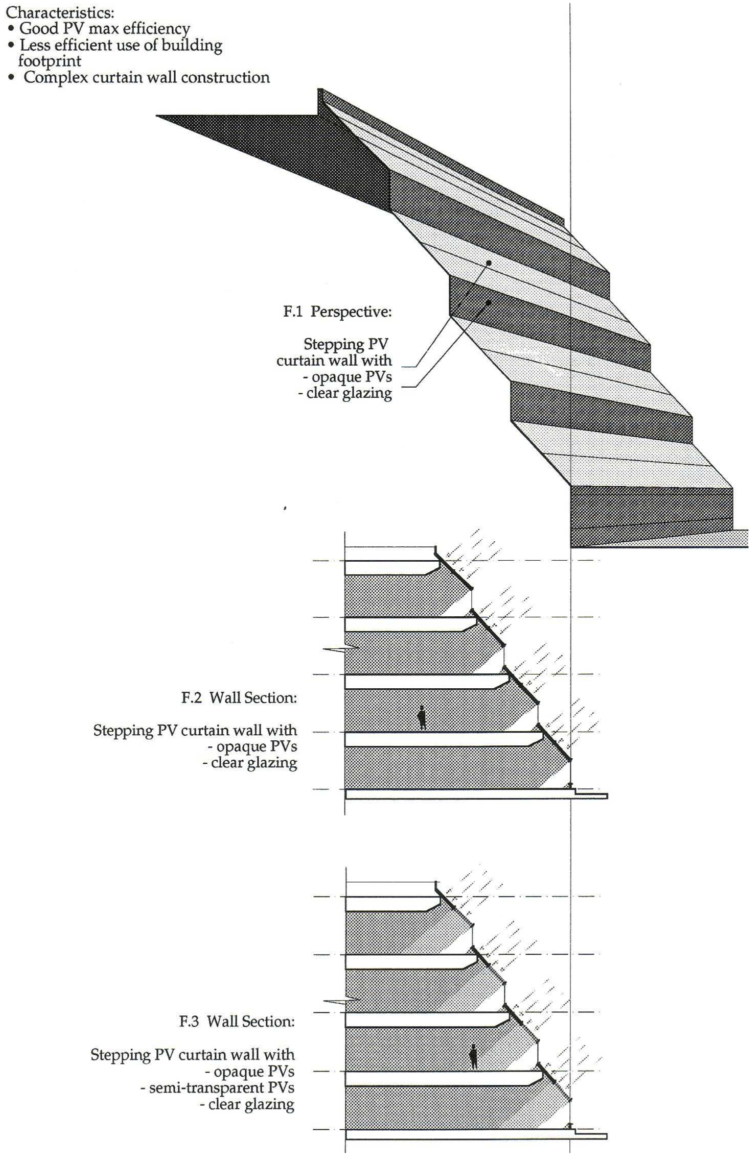

(b)

Figure 1.6.2.2.3 Applications of Photovoltaics onto building walls: (a) PV slopping curtain wall i.e. PV system are integrated into the slopped wall with opaque PVs and semitransparent PVs, (b) PV slopping/stepped curtain wall i.e.slopping/stepped curtain wall contains opaque PVs or semi transparent PVs (Sick and Erge, 1996).

1.7 Ventilated PV Panel Façade

Only a part of the solar energy spectrum absorbed by a PV material is converted into electrical energy (compare figure 1.4.1 and figure 1.4.2 on page 23). The rest of the solar energy spectrum is converted into heat, resulting in increased solar cell temperature. Heat is transferred from the PV panel to an air space in a ventilated PV façade by convection and radiation. Air movement is determined by the buoyancy pressure difference between the top and the bottom of the duct. Radiative heat transfer transmits energy across the air gap. The net radiation absorbed by the otherwise unheated wall, is in turn, transferred to the air.

Solar radiation heats both the solar cells and the building envelope (Bloem and Ossenbrink, 1995). In cases where building ventilation is important, passive ventilation can be achieved using the "stack effect" where buoyant warm air rises, creating an upward air flow (Shaw et al., 1995). The stack effect can be employed to ventilate a space adjacent to the column of moving air by extracting air through louvers or windows. The extraction of heat from the PV modules also helps to reduce PV operating temperatures and thus improve operating efficiencies and output electrical power (Watt et al., 1998b).

A composite Trombe-Michel wall illustrated in figure 1.7.1 was modelled for a PV panel integrated into building facade (Zrikem and Bilgen., 1987; Mootz and Bezian, 1996). Air is drawn in through the inlet section, heated by solar radiation in the convection channel and discharged through the outlet section. Additional heat is delivered to the adjoining room by conduction through the solar PV panel and the insulation.

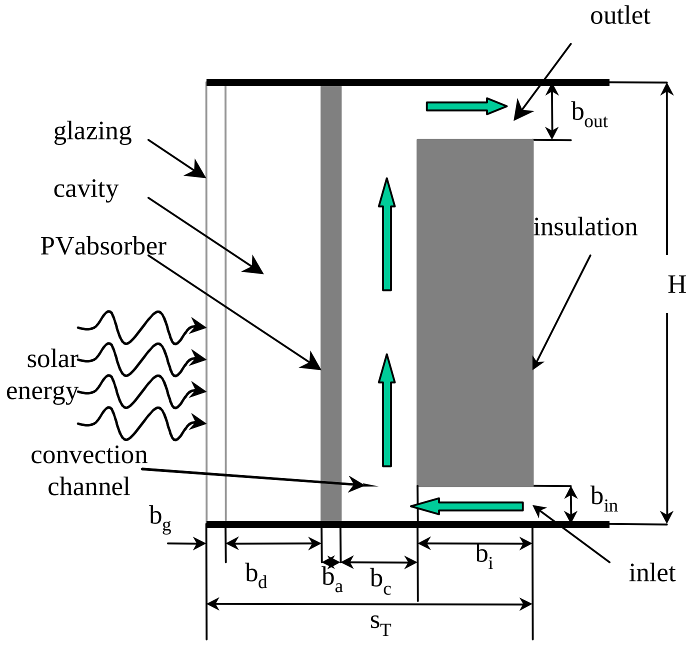

Figure 1.7.1 Model for PV panel integrated into a building facade (Mootz and Bezian, 1996).

The thermal efficiency of the system is described (Mootz and Bezian, 1996) by;

$$\eta = \frac{1}{GH}\left(\int_{0}^{b_{in}} \rho u C_1 T dy + \int_{H-b_{out}}^{H} \rho u C_1 T dy + U_{\text{int}} \int_{b_{in}}^{H-b_{out}} (T - T_{\text{int}}) dy \right)\Bigg|_{x=L} \tag{1.7.1}$$

The first two terms represent the convective losses i.e. the enthalpy difference of the air stream between the inlet and the outlet section and the third term corresponds to the conductive contributions to the heat losses from the back of the panel. The heat losses through the solar PV panel during non-recovery periods (Mootz and Bezian, 1996) are:

$$K = \frac{U_{\text{int}}}{H\left(T_{\text{int}} - T_{ext}\right)} \int_{0}^{H} \left(T_{\text{int}} - T\right) dy \Big|_{x=L} \tag{1.7.2}$$

An optimised heat loss coefficient of 0.7 $Wm^{-2}K^{-1}$ for a convection channel space width of 15-mm was reported. The best electrical PV panel performance during convective heat recovery periods required maximum channel spacing (Mootz and Bezian, 1996). A variable channel spacing proved to be the most efficient solution for both convective heat recovery and non-recovery periods.

1.7.1 Pressure Drop Across a Ventilated PV Façade

In a one-dimensional ‘loop analysis’ as shown in the figure 1.7.1.1, buoyancy forces are balanced by the pressure drops due to the friction at the entrance and exit for a naturally ventilated PV cladding element for building applications (Brinkworth et al., 2000). The PV array is tilted at an angle of θ to the horizontal and the system analysed as a sequence of quasi-steady states.

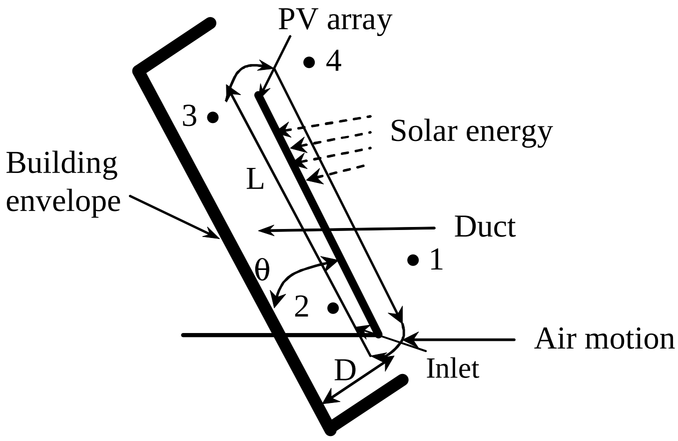

Figure 1.7.1.1 Schematic cross section of PV cladding (Brinkworth et al., 2000).

At the inlet (as shown in the figure 1.7.1.1) to the duct there is an entrance region, along which the flow adjusts from its initial state to fully developed flow conditions. At the entrance, the rate of pressure drop is greater than for fully-developed flow, due to the velocity gradient at the wall being higher initially, and to the increase in momentum flux as the velocity profile adjusts.

The pressure drop along the length L due to the internal friction along the path 2-3 in figure 1.7.1.1 becomes (Brinkworth, 2000a)

$$\Delta P = \mathrm{f}_{\text{app}} \left(\frac{L}{D}\right) \left(\frac{\rho U^2}{2}\right) \tag{1.7.1.1}$$

where the mean ‘apparent’ value f_{app} combines the values for both the duct and apertures.

The pressure difference equations along the loop (as shown in the figure 1.7.1.1) (Brinkworth, 2000a) is:

$$\begin{aligned} P_2 &= P_3 + \rho_m g L Sin(\theta) + \Delta P \\ P_1 &= P_4 + \rho_0 g L Sin(\theta) \end{aligned} \tag{1.7.1.2}$$

As the flow is incompressible, the Boussinesq approximation was used for the buoyancy term, so that (Brinkworth, 2000a)

$$(\rho_0 - \rho_m) = \rho_0 \beta (T_m - T_{in}) \tag{1.7.1.3}$$

1.7.2 **Flow Velocity Inside the Air Duct at the Back of a PV Panel**

An air duct channel of height 6.5 m exposed to a constant heat input was analysed and studied experimentally (Moshfegh and Sandberg, 1998). Rayleigh numbers for heat flux values of 20, 300 and 500 Wm^{-2} were presented as 2×10^8, 3×10^9 and 5×10^9 respectively. Turbulent flow was predicted when the heat input changed from 20 Wm^{-2} to 500 Wm^{-2}. Based on (i) a lumped parameter analysis for fully turbulent flow, (ii) the power law relationship between velocity and heat input, (iii) the relationship between the temperature rise at the outlet of the gap and the input heat was characterised by exponents equal to 1/3 and 2/3 respectively compared to predictions of 0.353 and 0.654. The flow velocity inside the duct was determined by (Moshfegh and Sandberg, 1998):

$$U_0 = \left(\frac{\alpha H}{A_i \psi}\right)^{\frac{1}{3}} B^{\frac{1}{3}} \tag{1.7.2.1}$$

where $B = \dfrac{g\beta q}{\rho C_p}$ (1.7.2.2)

and $\psi = \rho\left(\dfrac{1}{\rho_0} - \dfrac{1}{\rho_i}\right) + \dfrac{\lambda H}{d} + 0.5(1 + k_{entr})$ (1.7.2.3)

Using a single loop analysis, the flow inside the air duct at the back of the PV system was predicted and the flow rate determined using the buoyant driving forces and the sum of the pressure resistance as (Brinkworth, 2000b);

$$U = \sqrt{\frac{2s\beta gqDL}{0.5 \times k \times \left[\dfrac{f_{app} L}{D} + \sum k\right]}} \tag{1.7.2.4}$$

For zero wind velocity, flow through a PV ventilated stack is driven by buoyancy forces alone. In other cases the flow inside the duct becomes a mix of free and forced convection. In a long shallow duct flow is determined by internal flow resistance and the flow structure can be characterised by entrance lengths and the transition to turbulence. For a single vertical loop it was reported that the mass flow rate increased by 1.9 ms^{-1} when the heat input to the duct increased from 50 to 300 W (Brinkworth, 2000b).

1.7.3 Heat Transfer Inside an Air Duct at the Rear of a PV Panel

For a single crystal Si solar cell, a 14°C solar cell temperature increase decreases electrical efficiency by 0.6% (Moshfegh and Sandberg, 1998). An air gap at the rear of the photovoltaic system increases the heat transfer rate from the solar cells, decreases the solar cell temperature and therefore improves the solar cell performance. Air cooling ducts for building façade integrated photovoltaics are generally rectangular, but more complex trapezoidal shapes have been proposed (Brinkworth et.al., 2000). For an inclined air duct wall to which a PV element is mounted the temperature is (Brinkworth, 2000a)

$$T_w - T_m = \frac{q}{h} = \frac{qD}{kNu} \tag{1.7.3.1}$$

for uniform heat flux equation 1.7.3.1 becomes;

$$T_m - T_i = \frac{qx}{\rho c_p Ub} = \frac{2qxD}{k \Pr \mathrm{Re}_D} \tag{1.7.3.2}$$

A generalised form of Nu number for heat transfer into the air duct at the rear of the PV system is given by;

$$\overline{Nu} = \frac{\bar{h}D}{k} \tag{1.7.3.3}$$

The Reynolds analogy takes the general form (Brinkworth, 2000a);

$$\overline{Nu} = \frac{C_f}{2} \mathrm{Re} \quad \Pr^{\frac{1}{3}} = \frac{f}{8} \mathrm{Re} \quad \Pr^{\frac{1}{3}} \tag{1.7.3.4}$$

1.7.3.1 Long Wave Radiation Heat Transfer

Long wave electromagnetic energy radiation per unit area of a body at surface temperature T is given by the Stefan-Boltzmann law

$$q_{lwr} = \sigma \cdot \varepsilon \cdot T^4 \tag{1.7.3.1.1}$$

The fraction of isotropic radiation leaving one surface that reaches another surface is determined by the view factor (Incropera and DeWitt, 1996) defined as

$$F_{ij} = \tfrac{1}{A_i} \int_{A_i} \int_{A_j} \frac{\cos\theta_i \cos\theta_j}{\pi R^2} dA_i dA_j \tag{1.7.3.1.2}$$

The net long wave radiation exchange between surfaces i and j is given by

$$q_{lwr_{ij}} = A_i \cdot F_{ij} \cdot (q_i - q_j) = A_j \cdot F_{ji} \cdot (q_j - q_i) \tag{1.7.3.1.3}$$

A surface tilted at an angle $\beta_{surface}$ from the horizontal has a view factor of $(1 + \cos(\beta_{surface}))/2$ to the sky and $(1 - \cos(\beta_{surface}))/2$ to an horizontal surface (Liu and Jordan, 1963).

1.7.4 Thermal Regulation of a PV Panel

Radiation incident on to a PV surface, but not converted into electricity contributes to heat generation at the PV element. The thermal properties of PV elements are reported in terms of thermal resistance (Fuentes and Roaf, 1997). The temperature of the PV element can be calculated by (Watt et al., 1998a, 1998b, 1999)

$$T_{pv} = (1-\eta)\times(I_g)\times R_{th} \tag{1.7.4.1}$$

where the thermal resistance R_{th} has measured values shown in table 1.7.4.1.

Thermal resistance R_{th} (°C W^{-1} m^2)	Type of system	Reference
0.031	Roof integrated	Schmid, (1992)
0.022	Free standing module	Schmid, (1992)
0.052	Roof integrated modules	DeGheselle, (1997)
0.032	Vertical rainscreen cladding	Wilshaw et al., (1995)
0.035	Northumberland ventilated façade	Wilshaw et al., (1997)
0.042	Façade	Nordman et al., (1997)
0.024	Roof	Nordman et al., (1997)
0.042	Flue ventilated shingles	Okuda et al., (1994)
0.05	Closed flue	Okuda et al., (1994)
0.041	Ventilated roof integrated	Laukamp et al., (1995)
0.066	Non-ventilated façade integrated modules	Laukamp et al., (1995)

Table 1.7.4.1 Thermal resistance of different building integrated PV element.

Brinkworth et al., (1997) found that the upper most solar cell of a 0.485 m^2 solar panel was heated to 75°C at an ambient temperature 25°C with one sun insolation, reducing the efficiency from 14.5% by 10%. A generic PV wall and roof is shown in figure 1.7.4.1 (Brinkworth et al., 1997). It was observed that the peak temperature of the outer surface of the wall could be reduced from 50°C to 32°C by ventilation with a subsequent reduction in the heat gain to the building of 105.6 kJm^{-2}. The temperature gradient along the PV module in the vertical direction was 0.4 °Cm^{-1} and the air temperature had increased by 3°C by the top of the 1.5m tall air duct. A 15% electrical power improvement was reported by introducing the air duct. A simulation model was reported for the study of the thermal regulation of PV cladding resulting from airflow induced by buoyancy in a duct between the cladding and the wall (Brinkworth et al., 1997). The correlation between CFD predictions and Laser-Doppler anemometry (LDA) measurements for the airflow rate measurements was reported as approximately 0.96 (Brinkworth et al., 1997). Although the mean velocity of airflow was low (0.1 ms^{-1}), the reduction of cell operating temperature of between 15-20°C reported gave a significant increase in electrical conversion efficiency and reduction in building heat gain (Brinkworth et al., 1997).

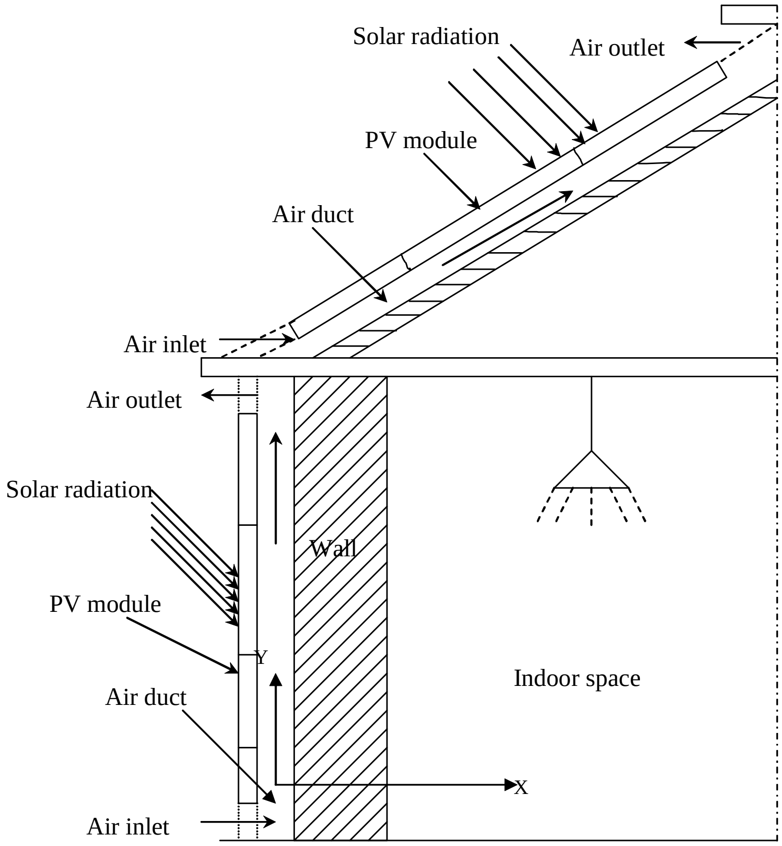

Figure 1.7.4.1 Schematic diagram of a generic modelled for thermal regulation of PV wall and roof (Brinkworth et al., 1997).

1.8 Conclusions

Concentrating solar energy systems can reduce system cost if the cost of the reflector system (and tracking system where applicable) is less than the replaced PV material cost. A concentrating panel separates the functions of light collection and conversion into electricity that are integrated in a flat photovoltaic panel (Luque, 1986). An advantage of concentrating panels is the tendency for solar cell efficiency to increase when the cell is under high irradiance. However concentrators for photovoltaic applications present some drawbacks when compared to flat PV panels as follows:

- The complexity of the tracking mechanism that may for remote applications (either geographically or in terms of façade accessibility), makes them less attractive (Luque, 1989).
- Inability at high concentration ratios to collect diffuse light, which limits their use in locations where high diffuse radiation prevails.
- Large size of the basic concentrator module (due to the need to spread the structure and tracking costs by producing a larger amount of electricity) as compared to flat panel is too large for small applications where photovoltaic electricity is cost-competitive today.
- High cost of the more sophisticated cells and the more complex structures used previously with concentrators jeopardizes the advantages obtained in cell area reduction.

- Increased solar cell temperatures decrease PV efficiency and differential heating (hot spot) increase mismatch errors.
- Lack of radiation uniformity giving use to mismatch errors.

These draw backs can be avoided by using a low concentration ratio asymmetric compound parabolic concentrator (ACPC) for photovoltaic applications. In cloudy and overcast sky conditions, an ACPC accepts a significant component of the diffuse solar radiation because of its high acceptance-half angle (Mills and Giutronich, 1978).